

# Aircraft-derived particle fluxes distinguish entrainment zone and decoupled layer nucleation in marine boundary layers

Ajmal Rasheeda Satheesh<sup>1</sup>, Markus D. Petters<sup>2</sup>, and Nicholas Meskhidze<sup>1</sup>

<sup>1</sup>Department of Marine, Earth, and Atmospheric Sciences, North Carolina State University, Raleigh, NC 27695, USA.

<sup>2</sup>Department of Chemical and Environmental Engineering, University of California, Riverside, CA 92521, USA.

Corresponding author: Nicholas Meskhidze (nmeskhidze@ncsu.edu)

## Abstract

3–10 nm sized particles, defined as "small particle event" (SPE), play a critical role in marine boundary layer aerosol budgets and aerosol–cloud interactions, yet the vertical distribution of their sources remains poorly constrained. We identified the vertical location of SPEs by deriving turbulent fluxes of 3–10 nm particles from aircraft measurements during the Aerosol and Cloud Experiments in the Eastern North Atlantic (ACE-ENA) campaign. To overcome stationarity limitations of traditional eddy covariance methods, we applied continuous wavelet transform analysis to data collected during June–July 2017 and January–February 2018 flights over the Azores. Our flux-based analysis revealed two distinct SPE scenarios with different vertical structures and spatial extents. The first featured nucleation in the entrainment zone, where free tropospheric air entrains into the boundary layer. The second showed nucleation in the decoupled layer, a stratified region between the well-mixed surface layer and cloud-topped upper boundary layer. In both cases, convergence of air masses from different layers diluted preexisting aerosol surface area to very low levels, creating conditions favorable for nucleation and generating strong downward particle fluxes. SPEs occurred in 15% of flights, challenging prevailing theoretical expectations that new particle formation should rarely occur in marine boundary layers due to high condensation and coagulation sink capacity of sea spray aerosols. Aircraft-derived particle fluxes provide first observational constraints on the vertical location and source strength of likely nucleation regions in the remote marine boundary layer, improving aerosol source representations in climate models and reducing uncertainties in aerosol–cloud interactions.

## 1. Introduction

Cloud adjustments due to aerosols constitute one of the most significant uncertainties in climate modeling (Intergovernmental Panel on Climate Change (IPCC), 2023). The magnitude of anthropogenic aerosol radiative forcing over the industrial period is strongly influenced by the abundance and properties of natural aerosols (Andreae, 2007; Carslaw et al., 2013; Hoose et al., 2009; Meskhidze et al., 2011). While uncertainties in aerosol radiative forcing from different processes (emissions, long-range transport, new particle formation, and removal) vary spatially, marine boundary layer (MBL) cloud microphysical properties exhibit the highest sensitivity to aerosol changes (Bellouin et al., 2020; Zhang et al., 2024). Understanding how marine low level clouds and their radiative effects respond to changing aerosol load is important due to their extensive spatial coverage, low optical thickness, and low background cloud condensation nuclei (CCN) concentrations. The response of these clouds to changes in aerosol loading remains

34 poorly constrained and represents a key source of uncertainty in climate projections (Zhang et al., 2024).  
35 Consequently, understanding aerosol composition, dynamics, and the mechanisms controlling CCN number budgets  
36 within the MBL is critical for improving climate models and reducing predictive uncertainties. While freshly nucleated  
37 particles in the 3–10 nm size range must undergo substantial growth before reaching CCN-relevant sizes (>50–80  
38 nm), this growth pathway is well established in marine environments. At typical marine boundary layer growth rates  
39 of 1–3 nm hr<sup>-1</sup> (Ehn et al., 2010; Nieminen et al., 2018; O’Dowd et al., 2010; Zheng et al., 2018), newly formed  
40 particles can reach CCN sizes within 24–48 hours. This timescale is consistent with air mass residence times in the  
41 remote marine boundary layer (Kulmala et al., 2012; Zheng et al., 2021). Constraining the vertical location and flux  
42 magnitude of freshly nucleated particles therefore represents a critical first step toward understanding the full aerosol  
43 number budget in marine environments, including the ultimate contribution of NPF to CCN populations.

44 Previous studies have identified three primary aerosol sources in remote MBLs: (1) long-range continental transport  
45 (Logan et al., 2014), (2) downward mixing of particles formed in the free troposphere (FT) through new particle  
46 formation (NPF) mechanisms (Clarke et al., 2013), and (3) sea spray emissions (Quinn et al., 2017). NPF occurring  
47 either near the top of stratocumulus cloud decks within open-cell regions (Petters et al., 2006) or in the upper portions  
48 of mid-latitude MBLs (Zheng et al., 2021) has been suggested as an important in-situ aerosol source within the MBL.  
49 However, the difficulty in capturing actual nucleation events and determining their precise vertical location has led to  
50 the prevailing theoretical view that NPF should rarely occur in remote marine boundary layers over open oceans. This  
51 expectation is based on the high condensation and coagulation sink capacity of the remote MBL, which includes not  
52 only sea spray aerosols (Bates et al., 1998; Pirjola et al., 2000) but also accumulation-mode sulfate and organic  
53 particles entrained from the free troposphere (Yoon et al., 2001). Clouds further suppress NPF by scavenging Aitken-  
54 mode particles (Zheng et al., 2018), accelerating sulfate production on existing droplets through aqueous-phase SO<sub>2</sub>  
55 oxidation (Sanchez et al., 2021), and sequestering DMS oxidation products such as Hydroperoxymethyl thioformate  
56 (HPMTF) that would otherwise contribute to sulfuric acid formation (Novak et al., 2021). Independent corroboration  
57 of in-situ NPF over the eastern North Atlantic comes from the Azores Stratocumulus Measurements of Radiation,  
58 Turbulence and Aerosols (ACORES) campaign, which conducted helicopter-borne observations over Graciosa Island  
59 in July 2017, overlapping in time and location with the ACE-ENA campaign analyzed here. Siebert et al., (2021)  
60 reported frequent burst-like freshly nucleated particle events near the stratocumulus cloud top and in the free  
61 troposphere, while also noting that these particles did not grow to CCN-relevant sizes within the ~2-hour observation  
62 window. This outcome is expected given the 24–48 hour growth timescales discussed above. These concentration-  
63 based observations, however, could not determine the precise vertical location of the nucleation source regions,  
64 motivating the flux-based approach developed in the present study.

65 Determining the vertical origin of freshly nucleated particles, whether from the free troposphere, the interfacial layer  
66 near the marine boundary layer–free troposphere boundary, or the interface between the well-mixed marine boundary  
67 layer and decoupled layer, has critical implications for both fundamental understanding and climate modeling.  
68 Knowledge of where nucleation occurs is essential for understanding aerosol formation mechanisms and enabling  
69 climate models to accurately simulate aerosol number size distributions required for radiative calculations. Most  
70 atmospheric models have historically assumed that nucleation should be negligible in marine boundary layers, instead

71 predicting that particle formation would be favored at high altitudes where both temperature and aerosol surface area  
72 are substantially lower. However, traditional time-averaged aerosol concentration measurements from aircraft  
73 campaigns provide limited information about the precise vertical location where nucleation events occur. This  
74 limitation has prevented definitive identification of nucleation zones within the marine boundary layer and hampered  
75 efforts to constrain the relative importance of different aerosol sources to marine aerosol budgets. Without direct  
76 observational evidence of where particles form, climate models continue to rely on theoretical assumptions that may  
77 not accurately represent actual nucleation processes in marine environments.

78 To address this critical knowledge gap, vertical turbulent flux measurements of freshly nucleated 3–10 nm particles  
79 have emerged as particularly valuable tools for inferring the vertical location of likely nucleation source regions (Islam  
80 et al., 2022). The flux direction provides indirect evidence of the likely nucleation location: positive (upward) fluxes  
81 indicate nucleation below the aircraft, while negative (downward) fluxes suggest nucleation above the aircraft. This  
82 approach offers unprecedented spatial and temporal resolution for identifying nucleation zones that cannot be detected  
83 through conventional concentration measurements alone. In this study, we derive vertical turbulent fluxes of 3–10 nm  
84 particles using data collected during the Aerosol and Cloud Experiments in the Eastern North Atlantic (ACE-ENA)  
85 campaign. The campaign comprised two intensive operational periods (IOPs) – summer 2017 and winter 2018 –  
86 utilizing the G1 research aircraft from the DOE Atmospheric Radiation Measurement (ARM) program. By applying  
87 continuous wavelet transform techniques to high-frequency aircraft measurements, we provide the first flux-based  
88 observational constraints on the vertical distribution of likely NPF source regions in remote marine boundary layers,  
89 enabling improved representation of aerosol sources in climate models.

## 90 **2. Materials and Methods**

### 91 **2.1 Sampling Site**

92 The Department of Energy Atmospheric Radiation Measurement (DOE–ARM) Eastern North Atlantic (ENA) facility  
93 is positioned on Graciosa Island within the Azores archipelago, located in the northeastern Atlantic Ocean to the west  
94 of Portugal (Mather and Voyles, 2013). Air mass transport to this location follows four main pathways: (1) polluted  
95 outflow from North American sources, (2) continental emissions originating from northern European regions, (3)  
96 relatively clean Arctic air masses, and (4) air masses that recirculate within the Azores High pressure system (Wood  
97 et al., 2015; Zheng et al., 2018). The location is characterized by a low average annual aerosol optical depth (AOD)  
98 of 0.12 (Logan et al., 2014).

99 Data collection for this research occurred during the ACE-ENA field campaign, which included two intensive  
100 observation periods (IOPs): the initial period ran from June 21 to July 20, 2017, while the second period extended  
101 from January 15 to February 18, 2018 (Wang et al., 2019). All data from the ARM ENA site are publicly accessible  
102 through the ARM Data Discovery tool.

## 103 2.2 Instrumentation

104 This study utilized datasets from the ARM Aerial Facility (Schmid et al., 2014). The G-1 research aircraft was  
105 equipped with over 50 instruments for comprehensive measurements of aerosols, clouds, and atmospheric processes.  
106 Detailed information regarding flight patterns executed during the campaign can be found in (Wang et al., 2019).

107 Two Condensation Particle Counters (CPCs, models 3025A and 3772, TSI Inc.) with nominal 50% counting efficiency  
108 cutoff diameters of 3 nm and 10 nm, respectively, sampled through an isokinetic inlet exhibiting >90% efficiency for  
109 particles with aerodynamic diameters below 5  $\mu\text{m}$ . The concentration of 3–10 nm sized particles was calculated as the  
110 difference between these CPC measurements and is denoted as  $N_{3-10}$  throughout this paper. Since the measurements  
111 did not extend to particle sizes small enough to directly identify nucleation events, we follow (Islam et al., 2022) in  
112 using the term "small particle event" (SPE) to characterize these observations. The CPC 3772 operated at a constant  
113 1 LPM flow rate maintained by an external pump and critical orifice (Fan and Pekour, 2018), while the CPC 3025A  
114 sample flow rate was not actively controlled. Both flow rates remained stable across the sampling altitude range  
115 (Zheng et al., 2021). The airborne CPC configuration was validated for operation up to 4000 m altitude and across  
116 ambient relative humidity conditions of 0–90% RH. For a typical polluted environment ( $\sim 5000 \text{ cm}^{-3}$ ), CPC  
117 concentration measurements had an accuracy of 0.3 % (Kuang and Mei, 2019). All data used in this study passed  
118 instrument mentor specified quality control filters, which are distributed alongside the data.

119 Vertical wind speed ( $w$ ) was measured using the Aircraft Integrated Meteorological Measurement System probe  
120 (AIMMS–20, Aventech Research Inc.). The raw measurements define downward movement as positive; therefore,  
121 the sign was inverted to align with meteorological convention (positive values indicating updrafts and negative values  
122 indicating downdrafts). Although measurements were recorded at 20 Hz, they were downsampled to 1 Hz to match  
123 the temporal resolution of the CPC data acquisition.

124 Aerosol size distributions from 10 nm to 600 nm were characterized using a Fast Integrated Mobility Spectrometer  
125 (FIMS) (Kulkarni and Wang, 2006a, b). The FIMS provides size distribution measurements at 1-second temporal  
126 resolution with signal-to-noise characteristics suitable for detecting both remote continental and clean marine aerosol  
127 concentrations, as demonstrated in aircraft-based deployments (Kulkarni and Wang, 2006a, b; Olfert et al., 2008).  
128 Particles are charged within the instrument and separated by electrical mobility using an applied electric field. The  
129 separated particles are subsequently grown into supermicron droplets in a condenser and imaged with a high-speed  
130 camera. This approach enables the FIMS to deliver size distribution measurements comparable to those of Scanning  
131 Mobility Particle Sizers (SMPS), but at a significantly higher time resolution. This study employed an advanced FIMS  
132 configuration utilizing a spatially varying electric field that extends the measurement range from 10 nm to 600 nm  
133 (Wang et al., 2017b, a). Size distribution measurements were normalized to dry conditions; therefore, reported size  
134 distributions and number concentrations do not represent ambient humidity conditions. Cloud contamination filters  
135 were applied to prevent misclassification of cloud droplets as aerosol particles, with detailed filtering procedures  
136 described in the following section. FIMS-derived number concentration also served as a quality control flag for the  
137 CPC 3772. Since both instruments share an overlapping detection size range (10–600 nm for FIMS; >10 nm for CPC  
138 3772), their total number concentrations should be broadly comparable under normal operating conditions. CPC  
139 concentrations falling below 10% of the simultaneously measured FIMS concentration indicate a physically

140 implausible discrepancy inconsistent with real atmospheric variability, and were therefore excluded from analysis as  
141 likely instrument malfunctions.

142 A two-dimensional stereo probe (2D-S) was used to retrieve drizzle concentration. It uses shadowgraphy to measure  
143 size distribution of hydrometeor particles in the size range 15  $\mu\text{m}$  to 2.5 mm (Glienke and Mei, 2019). All data  
144 products are publicly available through the ARM DOE website with citations in the data availability section and have  
145 undergone quality control by instrument mentors. Additional technical details are available in the corresponding  
146 citations.

## 147 **2.3 Data Reduction**

### 148 **2.3.1 Droplet shattering and cloud contamination**

149 Droplet shattering represents a significant source of measurement contamination in airborne aerosol sampling studies.  
150 Weber et al., (1998) described this phenomenon as the fragmentation of cloud droplets during in-cloud measurements,  
151 which can produce artifacts as small as 3 nm that appear in sampling instruments. Similarly, Korolev and Isaac, (2005)  
152 documented comparable shattering effects with ice particles. While a detailed examination of the physical mechanisms  
153 behind droplet shattering lies beyond this study's scope, it is essential to filter such artifacts from our dataset to prevent  
154 misidentification of SPEs.

155 Cloud contamination was systematically detected and eliminated by calculating liquid water content (LWC) using the  
156 approach of Zheng et al., (2021), which utilizes droplet size spectra from the Fast Cloud Droplet Probe (FCDP). Visual  
157 data examination established a detection threshold of  $3 \times 10^{-3} \text{ g m}^{-3}$ , comparable to the  $10^{-3} \text{ g m}^{-3}$  threshold employed  
158 by Zheng et al., (2021). Data exceeding this LWC threshold were excluded from analysis.

### 159 **2.3.2 Time lag correction**

160 Accurate temporal alignment between the vertical wind speed measured by the AIMMS-20 probe and the particle  
161 concentration measured by the CPCs is essential for reliable flux calculations. Because these instruments were located  
162 at different positions on the aircraft, a time lag exists between the two signals that must be determined and corrected  
163 prior to flux calculation.

164 To confirm that the two CPCs sampled identical air masses simultaneously, Spearman correlation coefficients were  
165 calculated for concentration measurements from both CPCs after removing cloud shattering artifacts and excluding  
166 SPE periods. From the complete campaign dataset, 370 randomly selected seconds of data yielded an average  
167 Spearman correlation coefficient of 0.97 (Supplementary Figs. S1–S2), confirming adequate synchronization between  
168 the two concentration records. However, a high correlation coefficient alone does not determine the precise temporal  
169 offset between the two signals.

170 Lag times between the two CPC signals were determined individually for every 20-second interval (representing the  
171 time taken for the airplane to traverse 2 km) using covariance maximization, shifting one CPC relative to the other  
172 signal to identify the temporal offset that maximizes their covariance. A single fixed lag time across the entire  
173 campaign was not appropriate, given the variability in lag times observed across flight segments (Supplementary Fig.

174 S3). This approach was independently validated using pressure measurements from the isokinetic inlet and static  
175 pressure from the AIMMS-20 probe. The two pressure records yielded a Spearman correlation coefficient of 0.99,  
176 confirming that both instruments consistently sampled the same air mass with no systematic offset (Supplementary  
177 Fig. S5). Similarly, covariance maximization applied to the pressure records confirmed that no single lag time was  
178 appropriate across the full campaign (Supplementary Fig. S6), consistent with the CPC-based analysis and further  
179 supporting the use of individually determined lag times for each flux calculation period.

## 180 **2.4 Aerosol number flux calculations**

181 Flux measurement methods were originally developed for tower-based platforms, and their application to aircraft  
182 measurements introduces fundamental differences in sampling characteristics that must be carefully considered.  
183 Tower measurements provide continuous observations at fixed heights, capturing the complete turbulent eddy  
184 spectrum including low-frequency contributions essential for accurate flux estimates (Helbig et al., 2021; Sakai et al.,  
185 2001). Aircraft measurements, by contrast, sample different air masses as the platform moves horizontally, effectively  
186 trading temporal for spatial averaging (Desjardins et al., 1989).

187 Three interconnected challenges arise specifically for aircraft-based flux measurements. First, turbulent intensity in  
188 convective boundary layers increases with height above the surface layer before decreasing above  $0.3\text{--}0.4 z_i$  (where  $z_i$   
189 is the boundary layer height). Maintaining flux variance within 10% therefore requires measurement lengths of 100  
190 to  $10^4$  times the boundary layer height (Lenschow and Stankov, 1986), a constraint that becomes increasingly difficult  
191 to satisfy at the higher altitudes routinely sampled by research aircraft. Second, high aircraft speeds impose strict  
192 constraints on sensor response times: for an aircraft traveling at  $100 \text{ m s}^{-1}$ , a 1 Hz sampling system resolves eddies no  
193 smaller than 200 m, approaching the lower limit for capturing the dominant flux-carrying scales. The CPCs used in  
194 this study operate at 1 Hz, meaning that contributions from smaller eddies are not resolved and must be accounted for  
195 through flux loss corrections (Section 2.8). Third, and most critically for flux calculation, aircraft measurements are  
196 inherently non-stationary as the platform continuously moves through different air masses, meteorological conditions,  
197 and altitudes. Traditional eddy covariance methods assume stationarity over the averaging period, a condition that is  
198 difficult to maintain during aircraft sampling (Gioli et al., 2004).

199 To address this limitation, this study employs the continuous wavelet transform (CWT) method for flux derivation.  
200 The primary advantage of the CWT approach is that it does not require stationarity and eliminates the need for data  
201 detrending, thereby avoiding systematic errors that can arise from linear detrending procedures (Rannik and Vesala,  
202 1999). This study follows the CWT flux derivation method of (Torrence and Compo, 1998), described below.

203 The wavelet coefficient,  $W_N(a,b)$ , for a function  $x(z)$  which changes with height, is calculated as a function of both  
204 location (height for airborne measurements or time for ground-based measurements) and scale (frequency or  
205 wavenumber) through convolution with a wavelet function ( $\psi$ ):

$$206 \quad W_N(a,b) = \int_{-\infty}^{\infty} x(z) \psi_{a,b}(z) dz \quad (1)$$

207 where  $\psi_{a,b}(z)$  represents the wavelet function, controlled by the scale parameter ( $a$ ) and translation parameter ( $b$ ). The  
 208 scale parameter governs the wavelet frequency, while the translation parameter shifts it in the temporal domain. The  
 209 wavelet function is defined as:

$$210 \quad \psi_{a,b}(z) = \frac{1}{\sqrt{a}} \psi_0\left(\frac{z-b}{a}\right) \quad (2)$$

211 All wavelet functions are based on a “mother” wavelet,  $\psi_0$ . For this study, the Morlet wavelet is chosen as the mother  
 212 wavelet, which is the product of a plane wave with a Gaussian function (Torrence and Compo, 1998). Schaller et al.,  
 213 (2017) reported that the Morlet wavelet provides reliable results in flux analysis even when traditional eddy covariance  
 214 methods fail.

$$215 \quad \psi_0(\eta) = \pi^{-\frac{1}{4}} e^{i\omega_0\eta} e^{-\frac{\eta^2}{2}} \quad (3)$$

216 where  $\omega_0$  is the non-dimensional frequency (set to 6 for this study), and  $\eta$  is the non-dimensional time parameter and  
 217  $\eta = \frac{z-b}{a}$ , the first exponential term is the complex sinusoid, and the second exponential term is the Gaussian envelope.

218 Using this methodology, the vertical turbulent particle flux can be calculated according to (Schaller et al., 2017;  
 219 Torrence and Compo, 1998) as:

$$220 \quad \overline{w'(z)N'_{3-10}(z)} = \frac{\delta_t}{c_\delta} \times \frac{\delta_j}{L} \times \sum_{n=0}^{L-1} \sum_{j=0}^J \left[ \frac{W_N(a,b) \times W_w^*(a,b)}{a(j)} \right] \quad (4)$$

221  $c_\delta$ , the wavelet specific reconstruction factor is taken as 0.776, which is empirically derived for the chosen wavelet  
 222 (Schaller et al., 2017; Torrence and Compo, 1998),  $L$  represents the number of elements in the time series with  
 223 timestep  $\delta_t$  which is the inverse of frequency (1 Hz for this study),  $J$  is the maximum number of scales with  $\delta_j$  being  
 224 the space between each discrete scale (Schaller et al., 2017; Torrence and Compo, 1998).

$$225 \quad J = \delta_j^{-1} \times \log_2\left(\frac{L \times \delta_t}{s_0}\right) \quad (5)$$

226  $\delta_j$  was chosen to be 0.25 s (Schaller et al., 2017; Torrence and Compo, 1998), this value can be adjusted to get better  
 227 scale resolution at the expense of higher computational cost,  $s_0$  is the smallest scale of the wavelet taken as  $2\delta_t$ ,  $a(j)$  is  
 228 the scale parameter for the discrete scale calculated as:

$$229 \quad a(j) = s_0 \times 2^{j\delta_j} \quad j = 0, 1, \dots, J \quad (6)$$

230  $W_N(a,b)$  is the wavelet coefficient for the particle concentration signal, and  $W_w^*(a,b)$  is the complex conjugate of the  
 231 wavelet coefficient for the vertical velocity signal. Under stationary conditions, fluxes calculated using both CWT and  
 232 traditional eddy covariance methods should yield equivalent results, though agreement may vary in aircraft  
 233 measurements due to the presence of non-stationarities (Misztal et al., 2014; Wolfe et al., 2018).

## 234 2.5 Limit of Detection Determination

235 Spirig et al., (2005) demonstrated that calculating covariance at time ranges significantly larger than the integral time  
236 scale can quantify the precision of individual flux determinations. The integral time scale was calculated using the  
237 cross-correlation function between vertical wind  $w$  and 3-10 nm sized particle size concentration, using the method  
238 described by (Lenschow et al., 2000; Wulfmeyer et al., 2016). The cross covariance is given as:

$$239 A_{x,y}(\tau) = \text{cov}(x_t, y_{t+\tau}) \quad (7)$$

240 Where  $x_t$  and  $y_t$  are the two signals of interest, with  $y$  shifted by the lag time  $\tau$ . Now the cross covariance is fitted to a  
241 model of the form:

$$242 A_{\text{model}}(\tau) = v - k\tau^{\frac{2}{3}} \quad (8)$$

243 Where  $v$  and  $k$  are fitted parameters. The line is fitted till the first zero crossing of the cross covariance. And using  
244 this the integral timescale,  $I$  is calculated as:

$$245 I = \frac{2}{5} \left( \frac{v}{k} \right)^{3/2} \quad (9)$$

246 The median value of the integral timescale for the flux events was  $\sim 11$  seconds. The limit of detection (LoD) is  
247 defined as 1.96 times (95% confidence interval) the standard deviation of covariance between  $w$  and  $N_{3-10}$  when one  
248 of the signals is temporarily shifted with respect to the other. To estimate the precision of an individual flux  
249 determination, we followed Spirig et al., (2005) and examined fluctuation of the covariance function at time lags far  
250 away from the true lag. The standard deviations of the covariance function were calculated between 4500 to 5700  
251 seconds (corresponding to 45 to 57 km spatial displacement) before and after the peak fluxes. These lag times were  
252 selected to be much higher than the integral timescale of turbulence at all measurement heights. The limit of detection  
253 (LoD) is defined as 1.96 times (95% confidence interval) the standard deviation of covariance between  $w$  and  $N_{3-10}$   
254 when one of the signals is temporarily shifted with respect to the other. Signal shifts  $-10$  to  $+10$  seconds  
255 (corresponding to  $\pm 1$  km spatial displacement) are applied to ensure complete decoupling between the signals. Flux  
256 calculations are restricted to periods when the aircraft maintained horizontal, straight line flight segments to ensure  
257 reliable flux estimates and minimize the influence of aircraft maneuvers on turbulence measurements. The limit of  
258 detection is used as an absolute value and hence if a particular flux event is lower in absolute value compared to the  
259 LoD, they will not be considered for analysis.

## 260 2.6 Small particle events selection criteria

261 Establishing appropriate threshold values for new particle formation over tropical oceanic regions presents significant  
262 challenges due to sparse observational datasets and the intricate interactions between meteorological and chemical  
263 processes in these environments. Earlier studies have typically used concentration thresholds of  $10^3$  to  $10^4$  particles  
264  $\text{cm}^{-3}$  for ultrafine particles (3–25 nm) to distinguish nucleation events from background conditions. However, these  
265 criteria were primarily established based on observations from continental or mid-latitude marine environments (Dal  
266 Maso et al., 2005; Kulmala et al., 2012). Given that tropical marine regions are characterized by reduced background  
267 aerosol loadings and distinct precursor gas profiles relative to higher latitude zones, more conservative thresholds

268 (500–1000 particles  $\text{cm}^{-3}$ ) may prove better suited for detecting nucleation phenomena in these relatively unpolluted  
 269 environments (Modini et al., 2009; Weber et al., 1997). Additionally, the aircraft-based measurement method  
 270 prevented the implementation of traditional nucleation event identification criteria, specifically the requirement for  
 271 persistent concentration increases spanning 1–2 hours to distinguish genuine nucleation from brief local source  
 272 influences (Kulmala et al., 2012).

273 For this study, we modified the methodology established by Zheng et al., (2021) to detect small particle  
 274 events (SPEs). Individual 1-second measurements were used to identify when  $N_{3-10}$  concentrations exceeded  $150 \text{ cm}^{-3}$ ,  
 275 once identified the measurements that exceeded the threshold were grouped into 10-second intervals (equivalent to  $\sim 1$   
 276 km spatial resolution), and the average  $N_{3-10}$  for the group was checked to see if it achieved statistical significance  
 277 using:

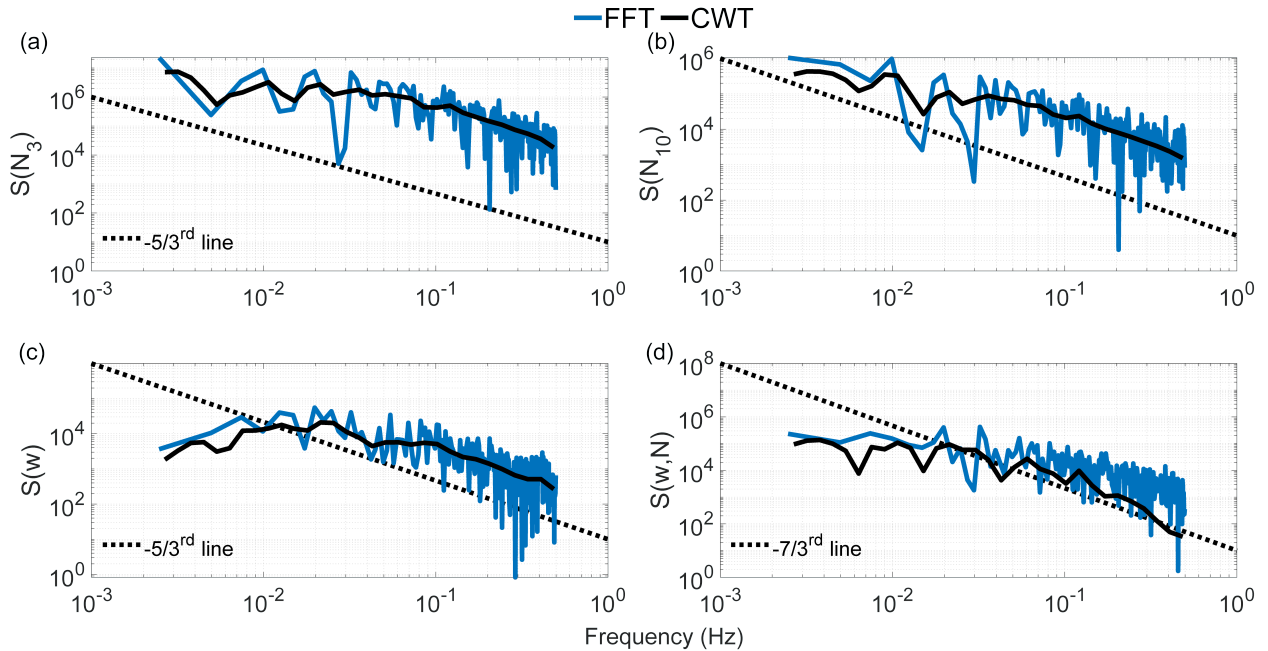
$$278 \quad N_3 - N_{10} > 3\sigma_D \quad (10)$$

279 where  $\sigma_D$  represents the uncertainty in the concentration difference between  $N_3$  and  $N_{10}$ , expressed as:

$$280 \quad \sigma_D = \sigma(N_3 - N_{10}) \quad (11)$$

## 281 2.7 Frequency response and flux averaging time

282 Momentum, enthalpy, and matter are transported in the atmosphere by eddies of different spatial scales. One-  
 283 dimensional power spectral analysis is used to decompose the signal into components of different frequencies, which  
 284 are associated with different eddy sizes. Fast Fourier Transform (FFT) and Continuous Wavelet Transform (CWT)  
 285 were used to calculate the power spectral density (PSD) of vertical wind speed and particle concentration.



286

287 **Figure 1. Power spectral density for (a)  $N_3$ , (b)  $N_{10}$ , (c) vertical wind velocity, and (d) 3-10 nm particle flux.**

288 Figure 1 shows the PSD for a flight leg on 21 June 2017 between 13:43 and 13:49 UTC at a height of 550 m above  
289 mean sea level. Dashed lines represent the theoretical slopes for the inertial subrange, which describe how energy  
290 cascades from larger to smaller eddies and finally dissipates as heat due to viscous friction (Pope, 2000). Both particle  
291 concentration spectra (Figs. 1a,b) and the flux spectrum (Fig. 1d) broadly follow the theoretical  $-5/3$  and  $-7/3$   
292 Kolmogorov scaling across the resolved frequency range. The supplementary figure comparing 1 Hz and 10 Hz  
293 vertical wind velocity spectra (Supplementary Fig. S7) confirms that turbulent energy exists at scales beyond the 1 Hz  
294 Nyquist frequency. The absence of a visible noise floor in the particle concentration spectra at high frequencies reflects  
295 the band-limited response of the CPC, which acts as a low-pass filter that attenuates high-frequency concentration  
296 fluctuations, producing a steep spectral roll-off rather than a white noise floor. While this results in a cleaner spectrum  
297 visually, it still represents real flux loss at high frequencies that is accounted for through the correction described in  
298 Section 2.8.

299 Figure 1 also shows some differences between FFT and CWT flux calculations, especially for fluxes at high  
300 frequencies. These differences are attributable primarily to non-stationarity in the aircraft data, as the platform moves  
301 through different air masses, meteorological conditions, and altitudes. FFT assumes stationarity over the entire  
302 analysis window and can therefore introduce artifacts under such conditions, whereas CWT provides time-localized  
303 frequency information that is more robust for non-stationary signals (Schaller et al., 2017). Li et al., (2023) evaluated  
304 uncertainties of turbulent flux calculation using both methods, finding that biases can range from 50–100% of the  
305 spectrally complete flux. We note that the high-frequency deviations visible in the particle concentration spectra are  
306 not a consequence of FFT limitations but reflect the band-limited response of the CPC, which attenuates concentration  
307 fluctuations at frequencies above  $\sim 0.3$  Hz, as discussed in Section 2.8. The CWT's more conservative high-frequency  
308 response may better represent the actual resolvable flux contributions (Misztal et al., 2014).

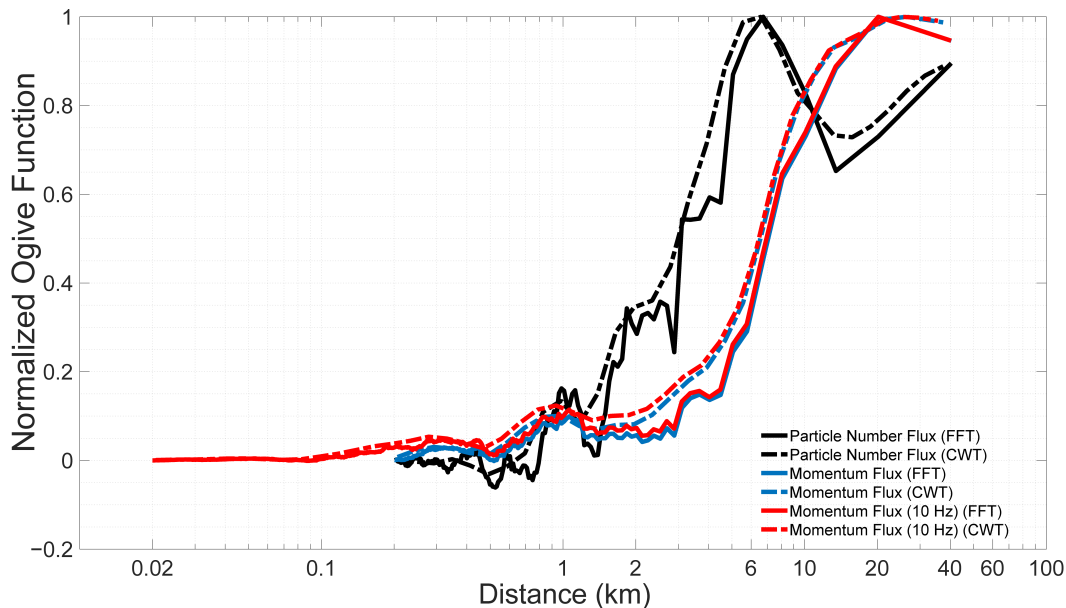
309 To assess whether the calculated fluxes adequately represent both low- and high-frequency turbulent contributions,  
310 we conducted ogive analysis using the approach described by Foken et al., (2006). Mobile measurement platforms  
311 necessitate modified considerations for flux averaging intervals. Standard 30-minute averaging periods used in  
312 stationary tower observations are inappropriate for aircraft measurements. Considering the aircraft's ground speed, a  
313 90-second sampling period covers an equivalent air mass to that sampled by a stationary sensor over 30 minutes at  
314 typical wind speeds of  $5 \text{ m s}^{-1}$ . To enable direct comparison between ogives computed using FFT and CWT methods,  
315 normalization was applied according to Sun et al., (2018):

$$316 \quad \widehat{Og}(f) = \frac{Og(f)}{\text{sgn}\{\max(Og(f)) + \min(Og(f))\} \max(|Og(k)|)} \quad (12)$$

317 where  $\text{sgn}\{x\}$  represents the signum function, returning +1 for positive  $x$ ,  $-1$  for negative  $x$ , and zero when  $x$  equals  
318 zero. When the normalized ogive equals 1, the ogive value corresponds precisely to the covariance value for that  
319 averaging period. The advantage of this normalization approach is that it facilitates the identification of cases where  
320 low-frequency turbulence has an opposite sign to high-frequency turbulence. In such situations, large and small eddies  
321 transport material in opposing directions, indicating complex atmospheric processes such as counter-gradient

322 transport. The normalized ogive plot visually reveals these opposing contributions through characteristic rise-and-fall  
323 patterns that might otherwise be obscured in non-normalized data.

324 Figure 2 illustrates the ogive as a function of distance covered by the aircraft for the same flight leg shown in Fig. 1.  
325 Signal frequency was converted to distance by dividing the aircraft speed (assumed to be constant at  $100 \text{ m s}^{-1}$ ) by the  
326 frequency obtained from the FFT or CWT analysis. This plot reveals that the particle flux for this flight leg can be  
327 resolved by averaging over 40 km. While both FFT and CWT ogives show agreement for this case, such consistency  
328 cannot be expected universally; therefore, CWT fluxes are used throughout this study for the reasons discussed in  
329 previous sections.



330

331 **Figure 2: Normalized ogive function as a function of distance covered by the aircraft. The ogive represents the cumulative**  
332 **fractional contribution to total flux from high to low frequencies.**

### 333 2.8 Flux loss correction

334 If the sensor used to measure fluxes are too slow to accurately capture the smaller eddies that contribute to the total  
335 flux, the turbulent fluxes will require correction. For micrometeorological flux measurements on towers at 10 m above  
336 the surface, instruments are typically operated at 10 Hz (Nyquist frequency = 5 Hz). Under typical wind speeds of 5  
337  $\text{m s}^{-1}$ , this sampling rate can resolve eddies as small as  $\sim 1 \text{ m}$ , ensuring that most energy-containing and inertial  
338 subrange eddies are captured (Aubinet et al., 2012; Lee et al., 2005; Stull, 1988).

339 However, airborne flux measurements present different challenges. The integral length scales of turbulent eddies  
340 increase approximately linearly with height within the surface layer (roughly the bottom 10% of the boundary layer),  
341 then remain approximately constant above this level, limited by the boundary layer height (Kaimal and Finnigan,  
342 1994). In the mixed layer portion of a typical boundary layer (above  $\sim 100 \text{ m}$  surface layer), integral length scales are  
343 typically 100-200 m (Lenschow and Stankov, 1986). At an aircraft ground speed of  $100 \text{ m s}^{-1}$ , the 1 Hz sampling  
344 provides 200 m spatial resolution, which approaches but does not fully resolve the integral length scale. Consequently,

345 the sampling resolution approaches the lower limit for adequately resolving the dominant flux-carrying scales and  
346 may under sample contributions from smaller turbulent structures.

347 To address this limitation, we applied the approximations from Horst (1997) to estimate the ratio of measured flux  
348 ( $F_m$ ) to spectrally complete flux ( $F$ ) for different atmospheric stability conditions encountered during campaign flights:

$$349 \frac{F_m}{F} = \frac{1}{1 + (2\pi n_m \tau_c \frac{\bar{u}}{z})^\alpha} \quad (13)$$

350 where  $F_m$  is the measured flux,  $F$  is the spectrally complete flux,  $\bar{u}$  is the magnitude of average wind speed,  $z$  is the  
351 height of the airplane,  $\tau_c$  is the response time constant of the CPC, which was taken as 3.0 s,  $\alpha =$  seven-eighths- and  $n_m$   
352  $= 0.085$  for neutral and unstable conditions (Pryor et al., 2007). Equation 13 was originally developed by Horst (1997)  
353 to estimate the attenuation of scalar flux measurements within the surface layer, but has been applied to aircraft  
354 measurements (Gioli et al., 2004), with corrected airborne fluxes showing good agreement with tower data when  
355 aircraft measurements were conducted over homogeneous surfaces at altitudes comparable to tower height.

356 To illustrate the practical importance of this correction, the  $\frac{F_m}{F}$  ratio varies substantially depending on measurement  
357 height and atmospheric stability conditions encountered during the campaign. For measurements conducted near the  
358 top of the marine boundary layer (~1,200–1,400 m) under near-neutral to unstable conditions,  $\frac{F_m}{F}$  values approach  
359 unity (0.93–0.99), indicating that flux losses are modest at these heights where the dominant flux-carrying eddies are  
360 large relative to the CPC response limitation. However, for measurements conducted closer to the surface (~30–550  
361 m),  $\frac{F_m}{F}$  values range from 0.70 to 0.95, implying that uncorrected fluxes could underestimate the spectrally complete  
362 flux by up to 30%. This highlights the importance of applying the flux loss correction, particularly for low-altitude  
363 flight legs where eddy sizes are smaller and the CPC response time constant becomes a more significant fraction of  
364 the dominant flux-carrying eddy turnover times.

365 Following the approach of Islam et al., (2022), we assessed the random uncertainty in particle flux due to counting  
366 statistics. We found it to be 2–3 orders of magnitude lower compared to the measured flux magnitudes reported in this  
367 study. Therefore, the correction due to discrete counting statistics of CPCs was not applied to this study.

### 368 **3.0 Results**

369 We examine two flight days as case studies of SPEs observed at varying altitudes above the ocean. Additional  
370 supporting flights are presented in the Supplementary Information. Table 1 summarizes the  $N_{3-10}$  vertical turbulent  
371 flux estimates derived from all six flight days analyzed in this study, grouped by the inferred nucleation regime. Flights  
372 1 and 2 (January 29 and February 10, 2018) are classified as entrainment zone nucleation events, where SPEs were  
373 detected near the top of the MBL at heights exceeding 1,200 m. Flights 3–6 (June 21 and July 7, 2017; February 18  
374 and 12, 2018) are classified as decoupled layer nucleation events, with SPEs observed across a broader range of  
375 altitudes (30–837 m). For all events, the ratio of measured flux to the spectrally-complete flux ( $\frac{F_m}{F}$ ) exceeds 0.76,  
376 indicating minimal flux loss due to sensor response limitations. The normalized vertical velocity variance ( $\sigma_w^2 w_*^{-2}$ )  
377 is generally low, consistent with relatively quiescent turbulent conditions during the measurement periods. Negative

378 flux values indicate downward transport of freshly nucleated particles from the entrainment zone toward the surface,  
 379 while positive values suggest upward transport from a source within the decoupled sub-cloud layer. Two of these  
 380 flight days, January 29, 2018 (Case 1) and June 21, 2017 (Case 2), are examined in detail as case studies in the  
 381 following sections, with the remaining four flights presented as supporting examples in the Supplementary  
 382 Information.

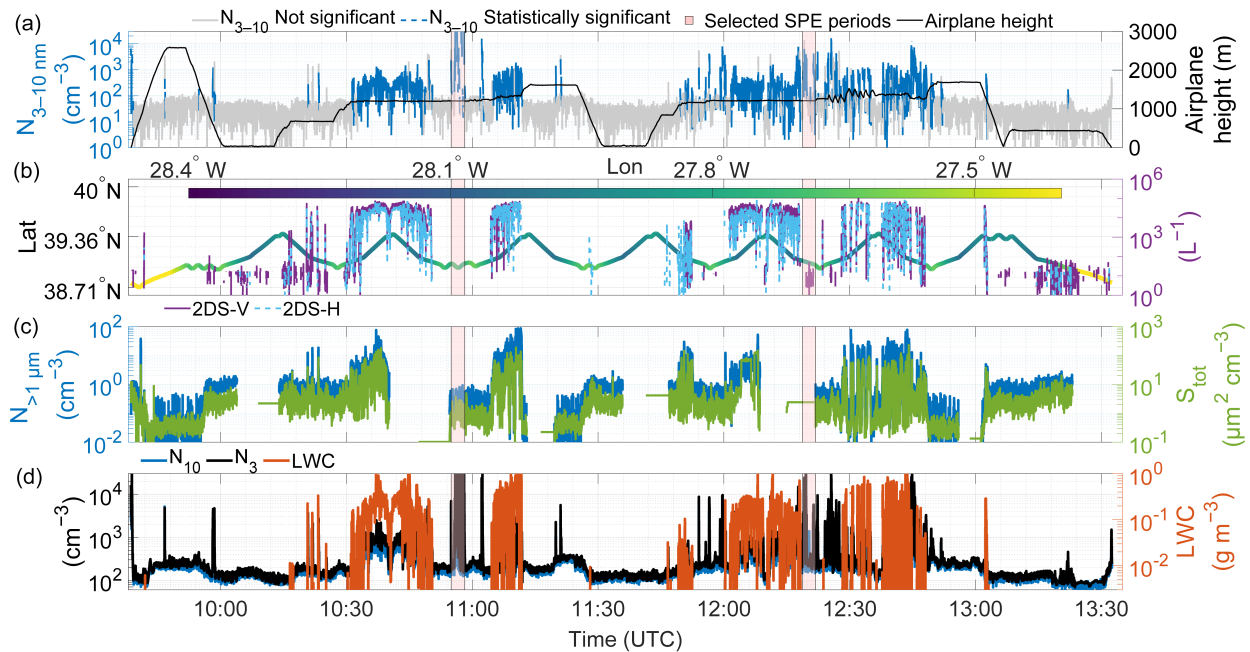
383 Table 1. Summary of  $N_{3-10}$  particle vertical turbulent flux estimates from aircraft campaigns with detection limits and  
 384 flux loss assessment.

No	Date	Time (UTC)	Height (m)	$N_{3-10}$ flux ( $\text{cm}^{-2} \text{s}^{-1}$ )	LoD ( $\text{cm}^{-2} \text{s}^{-1}$ )	$F_m/F$	$\sigma^2 w_*^{-2}$
<b>Entrainment zone nucleation</b>							
1	01/29/18	10:54:59-10:58:13	1,205	-41,092	34,423	0.97	0.01
		12:18:47-12:21:50	1,218	-2,975	2,085	0.98	0.005
2	02/10/18	13:53:20-13:55:02	1,375	-1,195	381	0.93	0.003
<b>Decoupled layer nucleation</b>							
3	06/21/17	14:03:30-14:09:25	800	1,139	294	0.99	0.016
		13:56:10-14:02:25	800	2,929	1,239	0.98	0.021
		13:42:40-13:49:23	550	-2,782	1,995	0.95	0.1
		13:32:20-13:38:40	30	-860	400	0.76	0.17
4	07/07/17	13:42:18-13:43:04	565	-94,093	49,410	0.86	0.02
		13:43:07-13:44:58	535	-21,317	4,959	0.90	0.031
5	02/18/18	14:17:32-14:19:38	555	298	115	0.81	0.016
		14:47:10-14:51:34	250	-3,217	1,153	0.70	0.056
6	02/12/18	14:54:27-14:58:37	837	5,433	1,173	0.93	0.04

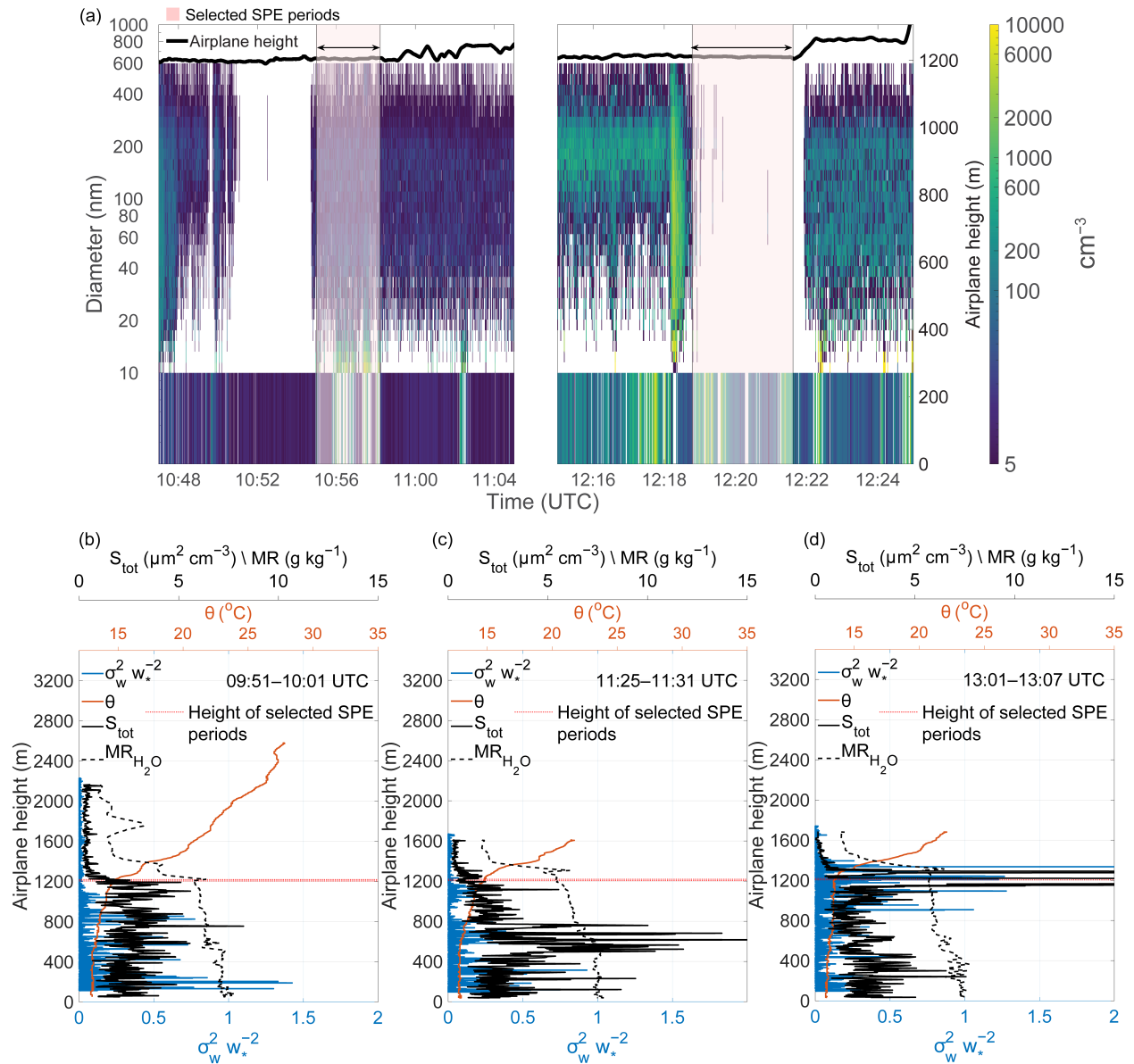
385

386 **Case 1: SPE occurring in the entrainment zone near the top of the marine boundary layer**

387 Figures 3–5 present data collected on January 29, 2018 with an additional example from February 10, 2018, shown in  
 388 Supplementary Figs. S8–S10. Back-trajectory analysis (not shown) indicates that the sampled air masses had been  
 389 circulating around the Azores for the preceding three days and were therefore likely less polluted than North American  
 390 outflow air masses. Figure 3 shows a multi-panel time series covering approximately 3.5 hours of flight operations.  
 391 The aircraft initially ascended to ~2,500 m but generally remained below ~1,500 m for most of the flight (Fig. 3a).  
 392 The flight trajectory (Fig. 3b) reflects predominantly east-west movement across the Azores region, spanning latitudes  
 393 from approximately 38.7° to 39.4°N and longitudes from -28.4° to -27.4°W. Drizzle number concentration measured  
 394 by 2DS (purple and blue lines in Fig. 3b) was absent or low during the selected SPE periods. Elevated drizzle number  
 395 concentration, together with high liquid water content regions (orange in Fig. 3d), mark frequent cloud encounters.  
 396 Following our quality control procedures, all  $N_{3-10}$  concentration data with  $LWC \geq 3 \times 10^{-3} \text{ g m}^{-3}$  were excluded from  
 397 analysis to avoid contamination from cloud droplet shattering artifacts. Pink-shaded periods mark the intervals chosen  
 398 for detailed analysis, which exhibited simultaneous increases in both  $N_3$  and  $N_{10}$  concentrations exceeding  $10^4 \text{ cm}^{-3}$   
 399 (indicating an SPE). Supermicron particle concentration (blue in Fig. 3c) as well as total particle surface area (green  
 400 in Fig. 3c) were also low during the selected SPE periods, indicating the absence of particles such as sea spray aerosols.  
 401



402  
 403 **Figure 3. Multi-parameter time series from the January 29, 2018 flight. (a)  $N_{3-10}$  particle concentrations and aircraft**  
 404 **altitude; (b) aircraft position (latitude and longitude) and drizzle number concentration; (c) supermicron particle**  
 405 **concentration and total particle surface area ( $S_{tot}$ ); (d) particle number concentrations ( $N_{10}$  and  $N_3$ ) and liquid water**  
 406 **content. Gaps in the time series indicate the missing data.**



407

408 **Figure 4. (a) Size-resolved particle number concentrations (10–600 nm) from FIMS as a function of time and**  
 409 **altitude, with  $N_{3-10}$  concentrations shown in the lower strip. Pink shading indicates selected SPE periods. (b-d)**  
 410 **Vertical profiles of potential temperature ( $\theta$ ), normalized vertical velocity variance ( $\sigma_w^2 w_*^{-2}$ ), total particle**  
 411 **surface area ( $S_{\text{tot}}$ ), and water vapor mixing ratio ( $\text{MR}_{\text{H}_2\text{O}}$ ) for three time periods nearest to the selected SPE**  
 412 **periods: (b) 09:51–10:01 UTC, (c) 11:25–11:31 UTC, and (d) 13:01–13:07 UTC. Gaps in the time series indicate**  
 413 **the missing data.**

414 Figure 4a shows the temporal evolution of particle concentration between  $\sim 10:47$ – $11:05$  and  $\sim 12:15$ – $12:25$  UTC. The  
 415 colormap represents FIMS-derived, size-resolved aerosol number concentrations (10–600 nm diameter), varying  
 416 across time and altitude, while the lower panel displays  $N_{3-10}$  concentrations. The two pink-highlighted intervals are  
 417 the same as in Fig. 3. The high particle concentration spike observed  $\sim 12:18$  UTC coincides with elevated LWC and  
 418 drizzle concentration (Fig. 3d) and was excluded from analysis following our quality control procedures (Section  
 419 2.3.1). Weber et al. (1998) documented that cloud droplet shattering can produce artificial particle concentrations as  
 420 small as 3 nm in airborne CPC measurements, making this the most plausible explanation for the observed spike.

421 Aircraft exhaust contamination can be ruled out, as the nearest prior flight transect over this region occurred  
422 approximately half an hour earlier at an altitude  $\sim 60$  m lower, more than sufficient time and vertical separation for  
423 complete plume dispersal. This data point was therefore excluded from all flux calculations as the concurrent LWC  
424 exceeded the quality control threshold of  $3 \times 10^{-3} \text{ g m}^{-3}$ .

425 Figures 4b–d present vertical profiles of potential temperature, normalized vertical velocity variance ( $\sigma_w^2 w_*^{-2}$ ) i.e.,  
426 (the vertical velocity variance normalized by the square of the convective velocity scale), total particle surface area,  
427 and the water vapor mixing ratio at three locations nearest to the pink-highlighted intervals. Sharp gradients in the  
428 potential temperature (orange) mark the top of the MBL, defining the capping inversion that suppresses vertical mixing  
429 between the boundary layer and the free troposphere. The co-occurrence of these temperature gradients with elevated  
430 normalized vertical velocity variance ( $\sigma_w^2 w_*^{-2}$ ) near the inversion level indicates the presence of an entrainment zone,  
431 where thermodynamic forcing (including cloud-top radiative cooling and wind shear) drives mixing between the free  
432 tropospheric air above and the convective boundary layer below (Boers and Eloranta, 1986). Figures 4b–d reveal a  
433 deep boundary layer with the entrainment zone between approximately 1,200–1,400 m, consistent with previous  
434 estimates that entrainment zones typically comprise 20–40% of boundary layer depth (Martin et al., 2014).

435 Figures 4b–d present the profiles of ( $\sigma_w^2 w_*^{-2}$ ) profiles, a metric that characterizes the intensity of turbulent structures  
436 in convective boundary layers (Deardorff, 1974; Dewani et al., 2023). These profiles show elevated ( $\sigma_w^2 w_*^{-2}$ ) values  
437 near the ocean surface and within the entrainment zone, with minimal values in the free troposphere, where significant  
438 turbulence is absent.

439 The water vapor mixing ratio profiles in Figs. 4b–d reveal evolving boundary layer moisture structure during the  
440 flight. The early profile (Fig. 4b) shows a relatively well-mixed moisture distribution below the capping inversion at  
441  $\sim 1,200$  m, with a sharp decrease into the drier free troposphere above. The latter profiles (Figs. 4c–d) exhibit a two-  
442 step moisture structure, with a sharper gradient near  $\sim 600$  m suggesting progressive decoupling of the boundary layer  
443 during the course of the flight, separating a moister surface layer from a drier sub-cloud layer above. Despite some  
444 vertical variability shown in Figs. 4b–d, the total particle surface area ( $S_{\text{tot}}$ ) remained relatively low throughout the  
445 flight, falling well below the campaign averages of  $\sim 30 \mu\text{m}^2 \text{ cm}^{-3}$  in the surface mixed layer and  $\sim 10 \mu\text{m}^2 \text{ cm}^{-3}$  in the  
446 upper decoupled layer reported by Zheng et al. (2021). Figure 4c also shows a distinct  $S_{\text{tot}}$  maximum at an altitude  
447 where small gradients in both potential temperature and mixing ratio suggest the presence of an entrainment layer.  
448 The pronounced  $S_{\text{tot}}$  increase could indicate a nucleation occurring at this location (see Case 2 below), although this  
449 hypothesis could not be independently verified looking at the  $N_{3-10}$  data in this case. Figure 4c shows that the  
450 entrainment zone and free troposphere were characterized with extremely low  $S_{\text{tot}}$  values.

451 Figure 5 presents the spatial distribution of  $N_{3-10}$  particle concentrations along the flight path at  $\sim 1,200$  m altitude  
452 (dashed lines in Figs. 4b–d), with the calculated vertical turbulent fluxes labeled at their respective measurement  
453 locations. Concentrations up to  $10,000 \text{ cm}^{-3}$  were observed along the flight track, with the highest values concentrated  
454 within a horizontal extent of less than 10 km. The substantial downward fluxes of  $N_{3-10}$  particles ( $-41,092$  and  $-2,975$   
455  $\text{cm}^{-2} \text{ s}^{-1}$ ) at  $\sim 1,200$  m both exceed their respective limits of detection (Table 1), confirming that the observed downward  
456 transport represents a statistically significant atmospheric signal rather than measurement noise. The downward flux  
457 direction indicates that the source of freshly nucleated particles was located above the measurement altitude, within

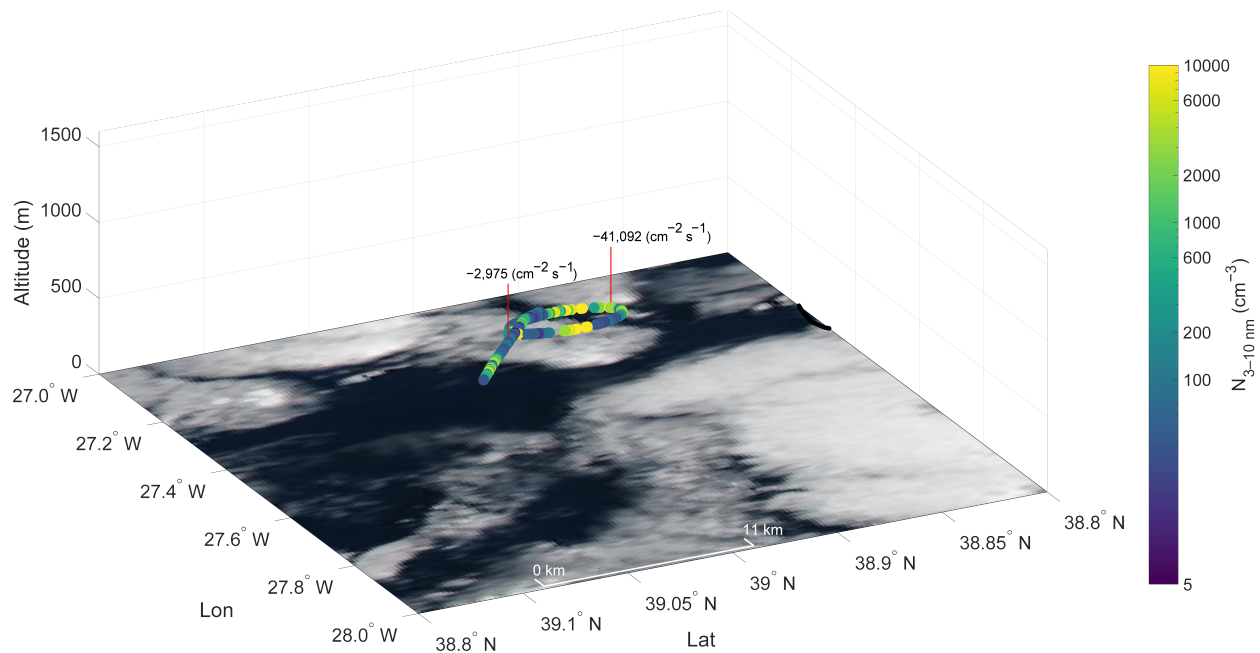
458 the entrainment zone, while the large difference in flux magnitudes between the two events likely reflects spatial  
459 heterogeneity in source strength and the proximity of the aircraft to the nucleation zone during each transect. This  
460 interpretation is supported by the near-absence of  $N_{3-10}$  at  $\sim 1,600$  m during 11:14–11:25 and 12:51–13:01 UTC (Fig.  
461 3), with the exception of brief concentration spikes of uncertain origin retained in the record due to insufficient  
462 evidence for their removal. The small particle size (3–10 nm) and limited horizontal extent of less than 10 km further  
463 argue against a free tropospheric nucleation source, as particles originating in the free troposphere would be expected  
464 to have grown substantially and the plume to have diluted during descent to measurement altitude.

465 Several mechanisms could promote nucleation specifically within the entrainment zone: adiabatic cooling in the rising  
466 convective plumes, turbulent fluctuation in temperature and vapor concentration generated by entrainment, and  
467 dilution of mixed-layer air by the entrained free tropospheric air, causing a sudden reduction in preexisting aerosol  
468 surface area (Nilsson et al., 2001). The extremely low  $S_{\text{tot}}$  values observed in the entrainment zone and free troposphere  
469 (Fig. 4), falling well below the campaign averages, are consistent with this interpretation. These conditions are  
470 analogous to those identified in previous studies linking entrainment zone nucleation to reduced condensation sink  
471 environments (Größ et al., 2018; Meskhidze et al., 2019; Nilsson et al., 2001). Supplementary Figs. S9 and S10 provide  
472 additional support, showing a downward flux of  $N_{3-10}$  particles ( $-1,195 \text{ cm}^{-2} \text{ s}^{-1}$ ) at 1,375 m with complete absence  
473 of  $N_{3-10}$  above  $\sim 1,400$  meters, consistent with SPE occurrence specifically within the entrainment zone between 1,375–  
474 1,400 m.

475 Figures 3–5 and the flux analysis (Table 1) demonstrate that the entrainment zone nucleation near the MBL top  
476 occurred on two days (January 29 and February 10, 2018), representing nearly 5% of flight days. Despite a relatively  
477 small horizontal extent ( $<10$  km), these newly formed particles can be entrained in the boundary layer via vertical  
478 turbulent processes, potentially playing an important role in marine aerosol number budget and, given sufficient time  
479 for growth to CCN-relevant sizes, potentially influencing cloud condensation nuclei concentrations for marine  
480 stratocumulus clouds.

481

482

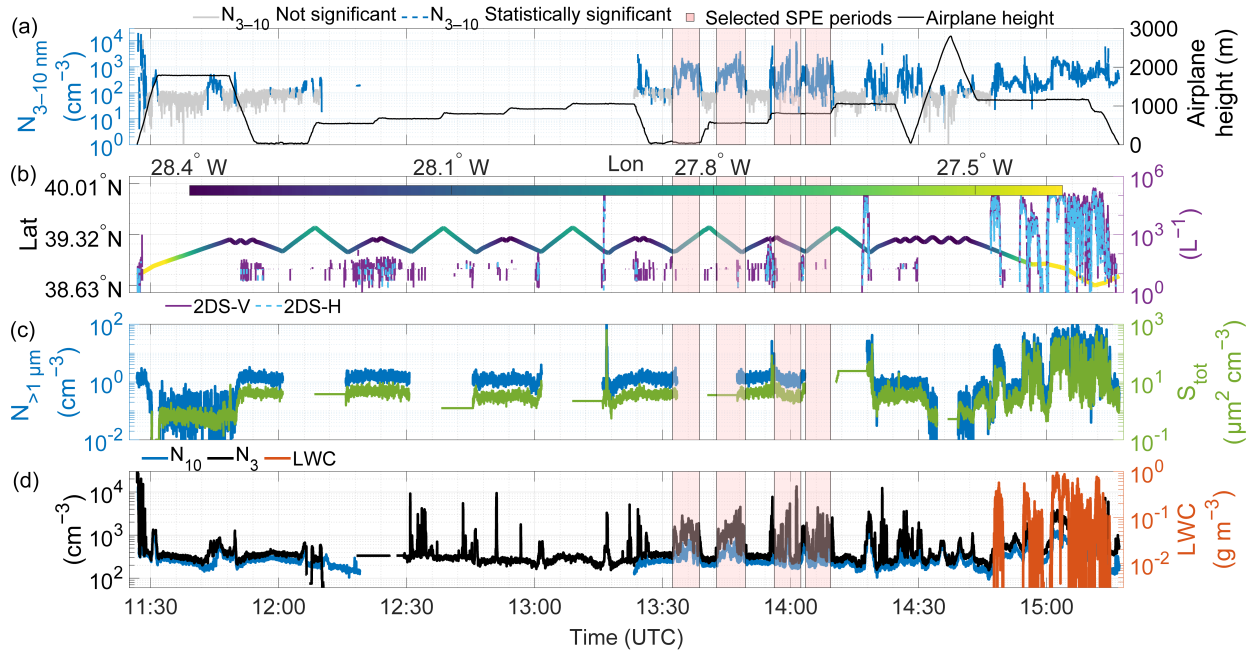


483  
484

485 **Figure 5. Spatial distribution of  $N_{3-10}$  particle concentrations along the flight track at ~1,200 m altitude during the period**  
 486 **highlighted in Figures 3 and 4. Calculated vertical turbulent fluxes are labeled at their respective measurement locations.**  
 487 **Color scale indicates  $N_{3-10}$  particle number concentrations ( $\text{cm}^{-3}$ ). The background shows a true-color satellite-corrected**  
 488 **reflectance image from the overpass at 15:15 UTC, with the ocean surface appearing dark and clouds appearing white.**  
 489 **Credit: NASA Worldview Snapshots.**

490 **Case 2: SPE occurring at the interface between the well-mixed surface layer and the decoupled layer**

491 Figures 6–8 present data from June 21, 2017, with additional examples from July 7, 2017, February 18, 2018 and  
 492 February 12, 2018, shown in Supplementary Figs. S11–S13, S14–16, and S17–S19. Back-trajectory analysis (not  
 493 shown) indicates that the sampled airmasses originated from the Arctic and were therefore expected to be relatively  
 494 clean. Figure 6 covers approximately 4 hours of flight operations, during which the aircraft initially flew at very low  
 495 altitudes (~30 and 50 m) near 12:00 and 13:30 UTC before gradually ascending to ~1,000 m. Drizzle number  
 496 concentration by 2DS (purple and blue lines in Fig. 6b) was absent or below the threshold during the selected SPE  
 497 periods. Multiple events with  $N_{3-10}$  concentrations from  $10^2$  to  $10^4 \text{ cm}^{-3}$  were observed throughout the second half of  
 498 the flight. The flight trajectory (Fig. 6b) reflects predominantly east-west movement, spanning latitudes from  
 499 approximately  $38.6^\circ$  to  $39.3^\circ\text{N}$  and longitudes from  $-28.4^\circ$  to  $-27.4^\circ\text{W}$ . Pink-highlighted intervals show periods with  
 500 concurrent increases in  $N_3$  and  $N_{10}$  concentrations exceeding  $10^3 \text{ cm}^{-3}$ , indicative occurrences of SPEs. As in Case 1,  
 501 supermicron particle concentrations (blue in Fig. 6c) and total particle surface area (green in Fig. 6c) remained low  
 502 during the selected SPE periods, indicating the absence of coarse-mode particles such as sea spray.  
 503

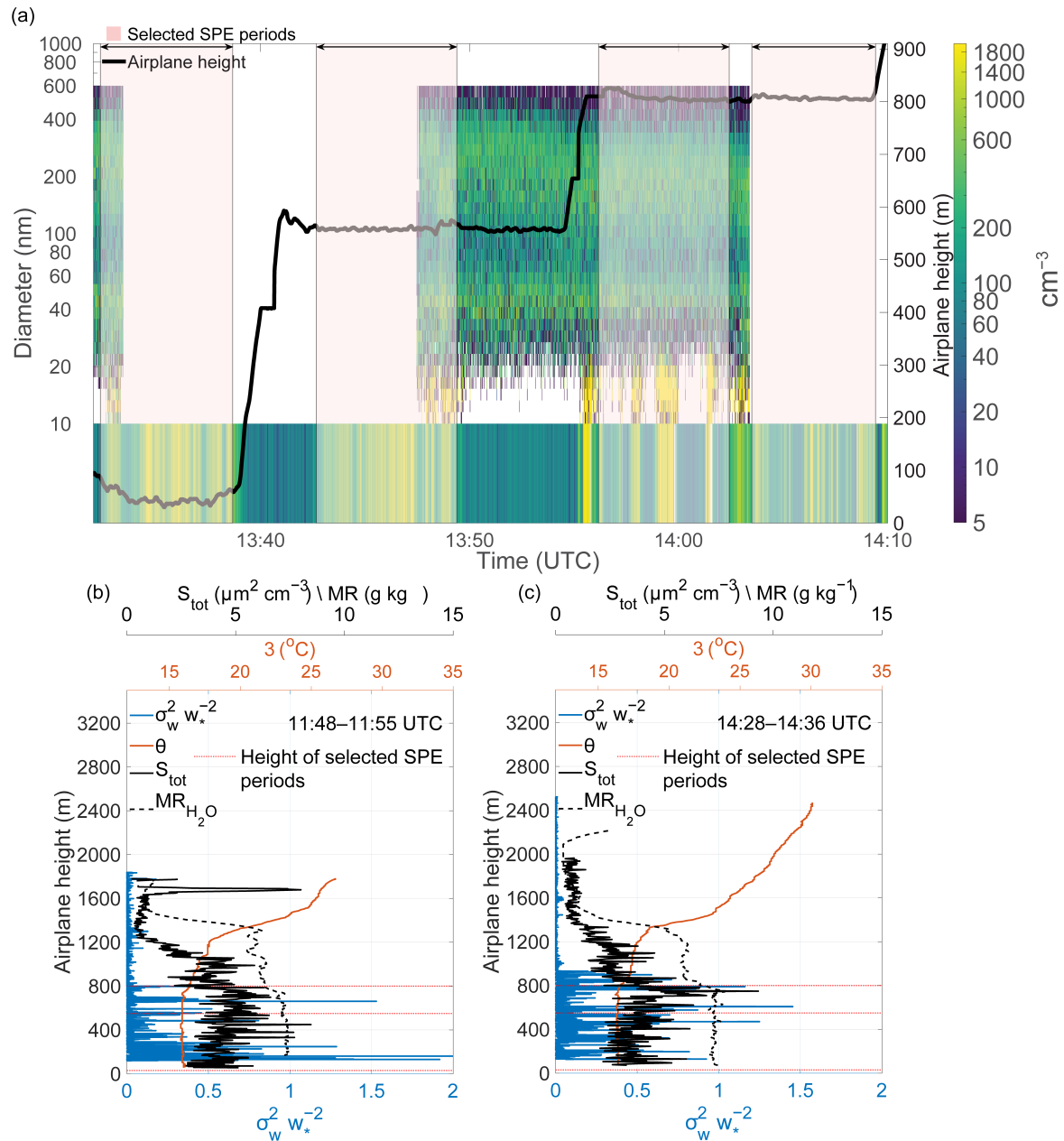


504

505 **Figure 6. Same as Figure 3 but for June 21, 2017. Gaps in the time series indicate the missing data.**

506 Figure 7a shows size-resolved particle number concentrations evolution during 13:30–14:20 UTC, encompassing the  
 507 four pink-highlighted intervals from Fig. 6. The panel Fig. 7a displays  $N_{3-10}$  particle concentrations. High  $N_{3-10}$   
 508 concentrations were encountered at multiple altitudes, with maximum values exceeding  $1,800 \text{ cm}^{-3}$  at  $\sim 800 \text{ m}$ .  
 509 The potential temperature and water vapor profiles (Figs. 7b,c) show the MBL structure consisting of a well mixed  
 510 surface layer extending to  $\sim 700 \text{ m}$  and a decoupled upper boundary layer between  $\sim 700\text{--}1300 \text{ m}$ . Decoupled  
 511 structures typically form from radiative heating of the cloud layer and evaporative cooling in the sub-cloud layer,  
 512 which stabilize the boundary layer and suppress vertical mixing (Galewsky et al., 2022; Jones et al., 2011; Wood and  
 513 Bretherton, 2004). Sharp gradients in both potential temperature and mixing ratio around  $1,300 \text{ m}$  marking the  
 514 entrainment zone, above which the free troposphere begins above  $1,400 \text{ m}$ . The  $(\sigma_w^2 w_*^{-2})$  profiles show higher  
 515 magnitudes in the mixed layer (indicating active turbulence) and low magnitudes in both the decoupled layer (due to  
 516 stratification and suppressed vertical mixing) and free troposphere. Total particle surface area remained low in the  
 517 mixed layer but increased considerably toward the top of the mixed layer before decreasing in the decoupled layer and  
 518 reaching very low values in the free troposphere.

519



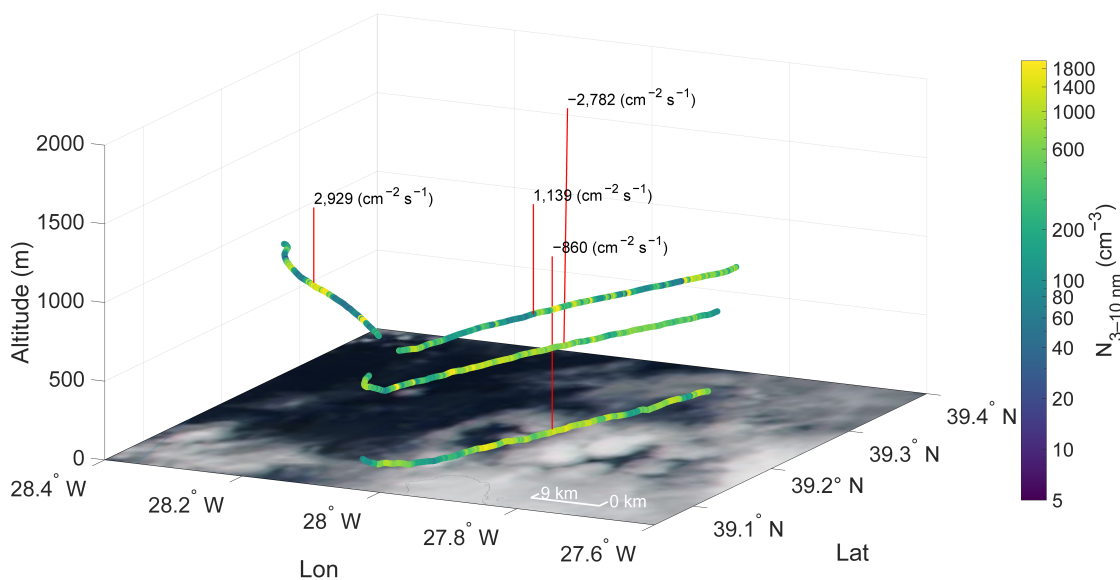
520  
521 **Figure 7. Same as Figure 4, but for June 21, 2017. Gaps in the time series indicate the missing data**

522

523 Figure 8 shows  $N_{3-10}$  particle concentrations along flight paths at varying altitudes: 30 m, 550 m, and two segments at  
524 800 m. We separated the 800 m path to prevent the airplane sampling the same airmass because from 13:55–14:03  
525 UTC the aircraft flew along the prevailing wind direction, then changed direction by 90° to fly perpendicular to the  
526 wind. The positive vertical turbulent fluxes at 800 and negative values below suggest the SPE occurred between 550–  
527 800 meters, likely at the top of the well mixed layer or the bottom of the decoupled layer.

528 The nucleation processes in the entrainment zone and at the base of the decoupled layer could be mechanistically  
529 similar. Both locations feature the convergence of distinct air masses, in this case, the well-mixed surface layer and

530 the stratified decoupled layer above, which generates turbulent mixing and aerosol dilution effects. While less  
 531 pronounced than at the boundary layer top, the interface between these layers exhibits comparable thermodynamic  
 532 conditions: potential temperature gradients, contrasting vapor concentrations, and localized adiabatic cooling. Figure  
 533 7 demonstrates that the decoupled layer maintains significantly lower aerosol surface area concentrations relative to  
 534 the well-mixed layer below, establishing conducive conditions for nucleation when air mass mixing occurs. A key  
 535 distinction, however, lies in the spatial characteristics, whereas entrainment zone nucleation showed limited horizontal  
 536 extent (<10 km), the decoupled layer event spanned at least 50–60 km, suggesting either more persistent favorable  
 537 conditions or a fundamentally different source mechanism operating over regional scales.



538

539 **Figure 8. Spatial distribution of  $N_{3-10}$  particle concentrations along the flight track at varying altitudes (30 m, 550 m, and**  
 540 **800 m) during the period highlighted in Figures 6 and 7. Calculated vertical turbulent fluxes are labeled at their respective**  
 541 **measurement locations. Color scale indicates  $N_{3-10}$  particle number concentrations ( $\text{cm}^{-3}$ ). The background shows a true-**  
 542 **color satellite reflectance image from the overpass at 14:15 UTC, with the ocean surface appearing dark and clouds**  
 543 **appearing white. Credit: NASA Worldview Snapshots.**

544 Figure 8 reveals a strong negative flux of  $N_{3-10}$  ( $-2,782 \text{ cm}^{-2} \text{ s}^{-1}$ ) at 550 m that is nearly three times greater  
 545 in magnitude than the flux at 50 m ( $-860 \text{ cm}^{-2} \text{ s}^{-1}$ ), likely due to particle evolution through growth and coagulation,  
 546 and dilution processes during vertical transport. The positive fluxes of  $N_{3-10}$  observed at 800 m ( $2,929$  and  $1,139 \text{ cm}^{-2}$   
 547  $\text{s}^{-1}$ ) suggest that nucleation initiated either at the top of the well-mixed boundary layer or at the bottom of the overlying  
 548 decoupled layer. This bidirectional flux structure suggests that newly formed particles were transported both upward  
 549 and downward from the formation zone through turbulent mixing. The comprehensive analysis presented in Figs. 6–  
 550 8, combined with the flux calculations in Table 1, provides some evidence that SPEs can originate within decoupled  
 551 layer structures, constituting a significant source of secondary marine aerosols in stratified boundary layer conditions.

#### 552 4. Discussion

553 This study demonstrates the value of vertical turbulent flux measurements for characterizing small particle events  
554 (SPE) in remote marine boundary layers. By deriving 3–10 nm particle fluxes from aircraft measurements during the  
555 ACE-ENA campaign, we identified two mechanistically distinct SPE scenarios that challenge conventional  
556 understanding of marine aerosol sources. Critically, while flux sign alone identifies the vertical location of the particle  
557 source, flux magnitude serves two additional essential roles: first, it must exceed the limit of detection to confirm that  
558 the observed directional transport represents a statistically significant atmospheric signal rather than measurement  
559 noise; and second, it provides quantitative constraints on source strength that cannot be obtained from sign alone.

560 Our analysis reveals different SPE mechanisms operating in the marine boundary layer. The first mode – entrainment  
561 zone nucleation – occurs at the boundary layer top (1,200–1,400 m) where several factors create favorable conditions:  
562 (1) dilution of mixed-layer air by entrained free tropospheric air causes sudden decreases in preexisting aerosol surface  
563 area, (2) adiabatic cooling in rising convective plumes reduces saturation vapor pressures, and (3) turbulent  
564 fluctuations in temperature and vapor concentration enhance nucleation rates (Größ et al., 2018; Nilsson et al., 2001).  
565 Strong downward fluxes (up to  $-41,092 \text{ cm}^{-2} \text{ s}^{-1}$ ) exceeding the limit of detection confirm that nucleation occurs  
566 specifically within this  $\sim 200$  m entrainment layer, while the absence of 3–10 nm particles above the entrainment zone  
567 rules out a free tropospheric source. The limited horizontal extent (2–9 km) of these events is consistent with the  
568 spatial scales of organized convective structures that develop in the upper decoupled marine boundary layer following  
569 cold front passages in the Azores region, where cumulus-associated drizzle reduces the condensation sink to levels  
570 favorable for nucleation (Etling and Brown, 1993; Zheng et al., 2021).

571 The large difference in flux magnitudes between the two entrainment zone events ( $-41,092$  vs.  $-2,975 \text{ cm}^{-2} \text{ s}^{-1}$ )  
572 provides information that flux sign alone cannot supply: it reflects spatial heterogeneity in source strength and the  
573 proximity of the aircraft to the nucleation zone during each transect. These flux magnitudes, integrated over the  
574 duration of the events, represent a substantial source of freshly nucleated particles to the marine aerosol number  
575 budget, constraints that can be used directly to evaluate nucleation parameterizations in regional and global models.  
576 While the ultimate contribution of these particles to CCN populations depends on growth timescales and loss processes  
577 during vertical transport (requiring  $\sim 24$ – $48$  hours at typical marine growth rates of  $\sim 1 \text{ nm hr}^{-1}$  to reach CCN-relevant  
578 sizes; (Zheng et al., 2021)), the flux-based constraints provided here represent a necessary observational foundation  
579 for quantifying this contribution in future studies.

580 Our analysis reveals a second distinct mode of SPE occurring within decoupled marine boundary layer structures,  
581 where particles originate at the interface between the well-mixed surface layer and the overlying decoupled layer  
582 ( $\sim 700$ – $800$  m altitude). While mechanistically similar to entrainment zone processes through air mass convergence,  
583 thermodynamic gradients, and aerosol dilution effects, decoupled layer nucleation occurs within the boundary layer  
584 structure rather than at its top, operating under conditions of reduced aerosol surface area concentrations and stratified  
585 vertical mixing. This mode exhibits a regional-scale horizontal extent ( $>50$  km) compared to the localized nature ( $<10$   
586 km) of entrainment zone events. The substantial negative flux magnitudes observed at intermediate altitudes ( $-2,782$   
587  $\text{cm}^{-2} \text{ s}^{-1}$  at 550 m) combined with positive fluxes aloft demonstrate active particle redistribution throughout the marine  
588 boundary layer. The factor of  $\sim 3$  difference in flux magnitude between the 550 m and 30 m levels ( $-2,782$  vs.  $-860$

589  $\text{cm}^{-2} \text{s}^{-1}$ ) is consistent with attenuation of the particle flux during downward transport through dilution with ambient  
590 air, as well as losses through coagulation and growth out of the 3–10 nm size range. This vertical divergence in flux  
591 magnitude represents a quantitative signature of particle evolution during transport that flux sign alone would be  
592 incapable of revealing. This mode represents a significant and previously underappreciated source of secondary  
593 marine aerosols that can efficiently contribute to regional aerosol budgets through direct incorporation into the surface  
594 mixed layer where particles undergo growth to cloud-relevant sizes.

## 595 **5. Conclusions**

596 The occurrence of newly formed particles in marine environments has been documented in a number of previous  
597 studies. Wiedensohler et al., (1996) observed sub-20 nm particles originating from the free troposphere or cloud tops  
598 within the MBL and mixed downwards over the open ocean, suggesting in-situ production based on correlations with  
599 absolute humidity. Covert et al., (1992) reported sub-20 nm particle production near precipitating cloud tops within  
600 the MBL, where larger particles acting as condensation sinks had been scavenged by precipitation, with sub-20 nm  
601 particles dominating 10% of the campaign and indicating episodic rather than continuous production. O'Dowd et al.,  
602 (2002) documented NPF events at the coastal Mace Head station when marine air masses encountered biogenic  
603 emissions from the intertidal zone. The ACORES campaign, conducted over the Azores at the same time as ACE-  
604 ENA, reported freshly nucleated particle bursts near the cloud top exceeding background MBL concentrations by  
605 more than an order of magnitude (Siebert et al., 2021). Concurrent helicopter-borne particle flux measurements over  
606 the Azores during ACORES (Lückerath et al., 2022) also documented particle fluxes in the marine boundary layer,  
607 providing complementary observational context to our aircraft-based approach. The prevailing theoretical framework,  
608 based on relatively high sea spray aerosol surface area acting as condensation and coagulation sinks (Bates et al.,  
609 1998; Pirjola et al., 2000), nonetheless predicted that NPF should rarely occur in remote marine boundary layers over  
610 open oceans. Our flux-based observations build on this existing framework by providing the first direct constraints on  
611 the vertical source location and strength of freshly nucleated particles in the remote marine boundary layer. Low  
612 aerosol surface area and specific meteorological configurations can create localized or regional zones where conditions  
613 become favorable. For entrainment zone and decoupled layer events, extremely low aerosol concentrations, combined  
614 with turbulent mixing and adiabatic cooling can create a transient "window" where nucleation can proceed despite  
615 moderate surface area concentrations lower in the boundary layer. Recent ground-based observations from the same  
616 campaign (Zheng et al., 2021) documented frequent NPF events but could not definitively determine vertical location.  
617 Our flux-based approach resolves this ambiguity by providing direct evidence of where particles originate relative to  
618 the measurement location. The negative (downward) fluxes in Case 1 unambiguously demonstrate an above-aircraft  
619 source, while the bidirectional fluxes in Case 2 indicate a distributed source encompassing the measurement altitude.  
620 These findings have important implications for understanding marine aerosol budgets. The spatial scales of these two  
621 SPE modes differ by an order of magnitude: entrainment zone events exhibited limited horizontal extents (<10 km),  
622 consistent with localized convective structures, while decoupled layer events spanned regional scales (50-60 km),  
623 suggesting fundamentally different formation mechanisms or persistence of favorable conditions. For the entrainment  
624 zone mode, while the aircraft sampled the SPE for only ~4 minutes during each transect due to its high ground speed,

625 NPF events in marine and continental environments are typically observed to persist for 2–5 hours (Kulmala et al.,  
626 2004; Zheng et al., 2021; Islam et al., 2022). Assuming the measured downward flux of  $-41,092 \text{ cm}^{-2} \text{ s}^{-1}$  is  
627 representative of a nucleation event of typical duration of  $\sim 3$  hours and using a mixed layer depth of  $\sim 1,200$  m, the  
628 estimated increase in vertically integrated particle number concentration is approximately:

$$629 \quad \Delta N_{3-10} \approx |F| \times \frac{\Delta t}{z_{MBL}} = \frac{41,092 \times 10,800}{1.2 \times 10^5} \approx 3,700 \text{ cm}^{-3}$$

630 where  $F$  is the flux in  $\text{cm}^{-2} \text{ s}^{-1}$ ,  $\Delta t$  is the event duration in seconds, and  $z_{MBL}$  is the mixed layer depth in cm. This  
631 represents a substantial addition to the total particle number concentration in the surface mixed layer, noting that this  
632 estimate refers to freshly nucleated 3–10 nm particles rather than CCN-relevant particles. The fraction surviving to  
633 CCN-relevant sizes ( $>50$ – $80$  nm) depends on growth rates and loss processes that cannot be quantified from single  
634 aircraft transects alone. However, Zheng et al. (2021) estimated that under favorable conditions at the same site, newly  
635 formed particles contributed on average  $\sim 50\%$  of total CCN concentrations following cold front passages, suggesting  
636 that even accounting for coagulation losses, the contribution of entrainment zone nucleation to the marine CCN budget  
637 may be substantial. Entrainment zone nucleation, despite its limited horizontal extent, may contribute significantly to  
638 the marine aerosol number budget through sustained downward transport via convective mixing. Though flux  
639 magnitudes for the decoupled layer nucleation events ( $-2,782 \text{ cm}^{-2} \text{ s}^{-1}$ ) are less pronounced, their large spatial extent  
640 likely results in comparable or larger aggregate contributions to regional aerosol budgets. We note that the  
641 contribution of freshly nucleated particles to CCN population depends on growth rates and loss processes during  
642 transport and cannot be assessed from short-term measurements alone. The flux magnitudes and vertical source  
643 locations reported here provide the observational foundation needed to evaluate this contribution quantitatively in  
644 future studies combining particle flux measurements with growth rate and CCN closure analyses.

645 Our observations, combined with the longer history of marine NPF observations cited above and recent  
646 ground-based measurements from the same campaign (Zheng et al., 2021), suggest that the contribution of in-situ  
647 marine boundary layer nucleation to the aerosol budget may be more significant than current model representations  
648 assume. Climate models have historically followed theoretical expectations that marine boundary layer nucleation  
649 should be negligible, instead representing new particles as primarily originating from free tropospheric entrainment  
650 or long-range continental transport (Clarke et al., 2013; Logan et al., 2014), with marine boundary layer nucleation  
651 treated as negligible. The frequent occurrence of SPE during the ACE-ENA campaign (entrainment zone nucleation  
652 in 2 and decoupled layer nucleation in 4 of 39 flights analyzed) suggests that marine boundary layer nucleation – in  
653 both modes – may be more climatologically important than previously recognized. Given that marine boundary layer  
654 cloud microphysical properties exhibit the highest sensitivity to aerosol changes (Bellouin et al., 2020; Zhang et al.,  
655 2024), and that even modest changes in CCN concentrations can substantially affect cloud radiative forcing in these  
656 pristine environments, proper representation of NPF sources is critical for reducing uncertainties in aerosol-cloud  
657 interaction estimates.

658 The continuous wavelet transform (CWT) approach proved essential for deriving reliable fluxes from fast-moving  
659 aircraft platforms. Traditional eddy covariance methods require stationarity conditions that are difficult to maintain  
660 during aircraft sampling, where the platform continuously moves through different air masses. The CWT method's  
661 ability to handle non-stationary data while avoiding systematic errors from linear detrending (Rannik and Vesala,

1999; Schaller et al., 2017) enabled flux calculations even during complex meteorological conditions. Our detailed analysis of frequency response and flux loss corrections demonstrates that 1 Hz CPC measurements, while not ideal, can resolve sufficient turbulent scales to capture the dominant flux contributions when proper corrections are applied. Importantly, flux magnitudes (not just flux sign) provide essential scientific value: they must exceed the limit of detection to confirm statistical significance, they constrain source strength and proximity, and they provide quantitative inputs for evaluating nucleation parameterizations in regional and global models. As the scientific community works to reduce uncertainties in aerosol-cloud interactions, flux-based approaches offer a promising path forward for understanding how, where, and when new particles form in Earth's remote marine atmosphere. Several limitations warrant acknowledgment. First, our 3–10 nm size range likely misses the initial nucleation at molecular cluster sizes (~1–3 nm), meaning we observe "small particle events" rather than nucleation itself. However, the rapid appearance of 3–10 nm particles with clear vertical structure in turbulent fluxes provides strong indirect evidence for nearby nucleation. Second, the aircraft's high ground speed (~100 m s<sup>-1</sup>) compared to typical tower-based measurements introduces challenges for capturing the full turbulent spectrum, particularly at lower altitudes where eddy sizes are smaller. Our flux loss corrections ( $F_m/F$  ratios of 0.70–0.99) account for this limitation but introduce additional uncertainty. Third, we cannot determine definitively the exact horizontal extent of NPF events from single aircraft transects, though crosswind sampling provides minimum extent estimates.

## Future Directions

This work establishes aircraft-derived aerosol fluxes as a valuable tool for characterizing marine boundary layer aerosol sources. Several directions would advance understanding:

**Slower aircrafts:** Unmanned aerial vehicles operating at 30–40 m s<sup>-1</sup> would better resolve small-scale turbulence, particularly near the surface, where flux loss corrections are currently largest, improving flux accuracy and enabling more detailed vertical structure analysis.

**Expanded measurements:** Simultaneous flux measurements of precursor gases (H<sub>2</sub>SO<sub>4</sub>, NH<sub>3</sub>, amines, organics) would directly test hypotheses about nucleation mechanisms and identify which chemical pathways dominate in different scenarios.

**Multi-aircraft coordination:** Coordinated measurements from more than one aircraft at different altitudes could directly observe vertical particle transport rates and evolution, constraining growth rates and loss processes during transit.

**Longer-term statistics:** Expanding beyond campaign-based measurements to seasonal or annual timescales would quantify the climatological importance of different NPF modes and their relationships to synoptic meteorological patterns.

**Model evaluation:** Using observed flux magnitudes and vertical source locations as benchmarks for evaluating marine boundary layer nucleation parameterizations in regional and global models would improve their representation of aerosol-cloud interactions and reduce uncertainties in aerosol indirect forcing estimates.

696 **Code availability**

697 All the scripts used to make the figures used in this study will be available along with the supplementary information

698 **Data availability**

699 All data from the ACE-ENA campaign are archived at the DOE ARM data center, covering measurements from the  
700 ARM Aerial Facility near ARM ENA site on Graciosa Island (June 15, 2017 - February 28, 2018).

701 ARM Aerial Facility (AAF) Merged VAP, <https://doi.org/10.5439/1999133>, (AAFMERGED, (Mei and Gaustad,  
702 2024)

703 ARM Aerial Facility (AAF) Merged aerosol size distribution, <https://doi.org/10.5439/1905541>,  
704 (AAFMERGEDAEROSOLSD,(Pekour and Ermold, 2017)

705 ARM Aerial Facility Isokinetic Inlet, <https://doi.org/10.5439/1241544>, (AAFINLETISOK, (Koontz et al., 2016)

706 ARM Aerial Facility (AAF) Aircraft Integrated Meteorological Measurement System (AIMMS) - Meteorological  
707 data, <https://doi.org/10.5439/1349241>, (AAFMETAIMS,(Matthews and Goldberger, 2020)

708 Interagency Working Group for Airborne Data and Telemetry Systems,  
709 <https://adc.arm.gov/discovery/#/results/s::aaf%20iwg/iopShortName::aaf2017ace-ena>, (IWG ACEENA)

710 Proton Transfer Reaction Mass Spectrometer (PTR-MS),

711 [https://adc.arm.gov/discovery/#/results/instrument\\_code::ptrms/iopShortName::aaf2017ace-ena](https://adc.arm.gov/discovery/#/results/instrument_code::ptrms/iopShortName::aaf2017ace-ena), (ACE ENA IOP1

712 G1 PTRMS)

713 **Author contribution**

714 ARS, MDP, and NM conceptualized the study. ARS performed the data curation, formal analysis, and designed the  
715 figures with contributions from MDP and NM. NM acquired the financial support for the project. ARS and NM wrote  
716 the paper, and all authors provided input on the paper for revision before submission.

717 **Competing interests**

718 The authors declare that they have no conflict of interest.

719 **Acknowledgements**

720 We acknowledge the Atmospheric Radiation Measurement (ARM) Climate Research Facility, a user facility of the  
721 United States Department of Energy (US DOE), Office of Science, sponsored by the Office of Biological and  
722 Environmental Research. We thank Dr. Jian Wang and all the staff responsible for the operation of the ACE-ENA  
723 campaign. We acknowledge the use of imagery from the NASA Worldview application, part of the NASA Earth  
724 Observing System Data and Information System (EOSDIS). AI tools were used to correct the spelling and sentence  
725 structure of the manuscript

726 **Financial support**

727 This work was supported by the DOE Office of Science, Biological and Environment Research, Grant No. DE-  
728 SC0024873

729 **References**

- 730 Andreae, M. O.: Aerosols Before Pollution, *Science*, 315, 50–51, <https://doi.org/10.1126/science.1136529>, 2007.
- 731 Aubinet, M., Vesala, T., and Papale, D. (Eds.): *Eddy Covariance: A Practical Guide to Measurement and Data Analysis*, Springer Netherlands, Dordrecht, <https://doi.org/10.1007/978-94-007-2351-1>, 2012.
- 733 Bates, T. S., Kapustin, V. N., Quinn, P. K., Covert, D. S., Coffman, D. J., Mari, C., Durkee, P. A., De Bruyn, W. J.,  
734 and Saltzman, E. S.: Processes controlling the distribution of aerosol particles in the lower marine boundary layer  
735 during the First Aerosol Characterization Experiment (ACE 1), *J. Geophys. Res. Atmospheres*, 103, 16369–16383,  
736 <https://doi.org/10.1029/97JD03720>, 1998.
- 737 Bellouin, N., Quaas, J., Gryspeerdt, E., Kinne, S., Stier, P., Watson-Parris, D., Boucher, O., Carslaw, K. S.,  
738 Christensen, M., Daniau, A. -L., Dufresne, J. -L., Feingold, G., Fiedler, S., Forster, P., Gettelman, A., Haywood, J.  
739 M., Lohmann, U., Malavelle, F., Mauritsen, T., McCoy, D. T., Myhre, G., Mülmenstädt, J., Neubauer, D., Possner,  
740 A., Rugenstein, M., Sato, Y., Schulz, M., Schwartz, S. E., Sourdeval, O., Storelvmo, T., Toll, V., Winker, D., and  
741 Stevens, B.: Bounding Global Aerosol Radiative Forcing of Climate Change, *Rev. Geophys.*, 58, e2019RG000660,  
742 <https://doi.org/10.1029/2019RG000660>, 2020.
- 743 Boers, R. and Eloranta, E. W.: Lidar measurements of the atmospheric entrainment zone and the potential temperature  
744 jump across the top of the mixed layer, *Bound.-Layer Meteorol.*, 34, 357–375, <https://doi.org/10.1007/BF00120988>,  
745 1986.
- 746 Carslaw, K. S., Lee, L. A., Reddington, C. L., Pringle, K. J., Rap, A., Forster, P. M., Mann, G. W., Spracklen, D. V.,  
747 Woodhouse, M. T., Regayre, L. A., and Pierce, J. R.: Large contribution of natural aerosols to uncertainty in indirect  
748 forcing, *Nature*, 503, 67–71, <https://doi.org/10.1038/nature12674>, 2013.
- 749 Clarke, A. D., Freitag, S., Simpson, R. M. C., Hudson, J. G., Howell, S. G., Brekhovskikh, V. L., Campos, T.,  
750 Kapustin, V. N., and Zhou, J.: Free troposphere as a major source of CCN for the equatorial pacific boundary layer:  
751 long-range transport and teleconnections, *Atmospheric Chem. Phys.*, 13, 7511–7529, <https://doi.org/10.5194/acp-13-7511-2013>, 2013.
- 753 Covert, D. S., Kapustin, V. N., Quinn, P. K., and Bates, T. S.: New particle formation in the marine boundary layer,  
754 *J. Geophys. Res. Atmospheres*, 97, 20581–20589, <https://doi.org/10.1029/92JD02074>, 1992.
- 755 Dal Maso, M., Kulmala, M., Riipinen, I., Wagner, R., Hussein, T., Aalto, P. P., and Lehtinen, K.: Formation and  
756 growth of fresh atmospheric aerosols: eight years of aerosol size distribution data from SMEAR II, Hyytiälä, Finland,  
757 *Boreal Environ. Res.*, 10, 323–336, 2005.
- 758 Deardorff, J. W.: Three-dimensional numerical study of turbulence in an entraining mixed layer, *Bound.-Layer*  
759 *Meteorol.*, 7, 199–226, <https://doi.org/10.1007/BF00227913>, 1974.
- 760 Desjardins, R. L., MacPherson, J. I., Schuepp, P. H., and Karanja, F.: An evaluation of aircraft flux measurements of  
761 CO<sub>2</sub>, water vapor and sensible heat, *Bound.-Layer Meteorol.*, 47, 55–69, 1989.
- 762 Dewani, N., Sakradzija, M., Schlemmer, L., Leinweber, R., and Schmidli, J.: Dependency of vertical velocity variance  
763 on meteorological conditions in the convective boundary layer, *Atmospheric Chem. Phys.*, 23, 4045–4058,  
764 <https://doi.org/10.5194/acp-23-4045-2023>, 2023.

- 765 Ehn, M., Vuollekoski, H., Petäjä, T., Kerminen, V., Vana, M., Aalto, P., de Leeuw, G., Ceburnis, D., Dupuy, R.,  
766 O'Dowd, C. D., and Kulmala, M.: Growth rates during coastal and marine new particle formation in western Ireland,  
767 *J. Geophys. Res. Atmospheres*, 115, 2010JD014292, <https://doi.org/10.1029/2010JD014292>, 2010.
- 768 Fan, M. and Pekour, M.: CPC\_ACEENA, <https://doi.org/10.5439/1440985>, 2018.
- 769 Foken, T., Wimmer, F., Mauder, M., Thomas, C., and Liebethal, C.: Some aspects of the energy balance closure  
770 problem, *Atmospheric Chem. Phys.*, 6, 4395–4402, <https://doi.org/10.5194/acp-6-4395-2006>, 2006.
- 771 Galewsky, J., Jensen, M. P., and Delp, J.: Marine Boundary Layer Decoupling and the Stable Isotopic Composition  
772 of Water Vapor, *J. Geophys. Res. Atmospheres*, 127, e2021JD035470, <https://doi.org/10.1029/2021JD035470>, 2022.
- 773 Gioli, B., Miglietta, F., De Martino, B., Hutjes, R. W. A., Dolman, H. A. J., Lindroth, A., Schumacher, M., Sanz, M.  
774 J., Manca, G., Peressotti, A., and Dumas, E. J.: Comparison between tower and aircraft-based eddy covariance fluxes  
775 in five European regions, *Agric. For. Meteorol.*, 127, 1–16, <https://doi.org/10.1016/j.agrformet.2004.08.004>, 2004.
- 776 Größ, J., Hamed, A., Sonntag, A., Spindler, G., Elina Manninen, H., Nieminen, T., Kulmala, M., Hörrak, U., Plass-  
777 Dülmer, C., Wiedensohler, A., and Birmili, W.: Atmospheric new particle formation at the research station Melpitz,  
778 Germany: connection with gaseous precursors and meteorological parameters, *Atmospheric Chem. Phys.*, 18, 1835–  
779 1861, <https://doi.org/10.5194/acp-18-1835-2018>, 2018.
- 780 Helbig, M., Gerken, T., Beamesderfer, E. R., Baldocchi, D. D., Banerjee, T., Biraud, S. C., Brown, W. O. J., Brunzell,  
781 N. A., Burakowski, E. A., Burns, S. P., Butterworth, B. J., Chan, W. S., Davis, K. J., Desai, A. R., Fuentes, J. D.,  
782 Hollinger, D. Y., Kljun, N., Mauder, M., Novick, K. A., Perkins, J. M., Rahn, D. A., Rey-Sanchez, C., Santanello, J.  
783 A., Scott, R. L., Seyednasrollah, B., Stoy, P. C., Sullivan, R. C., de Arellano, J. V.-G., Wharton, S., Yi, C., and  
784 Richardson, A. D.: Integrating continuous atmospheric boundary layer and tower-based flux measurements to advance  
785 understanding of land-atmosphere interactions, *Agric. For. Meteorol.*, 307, 108509,  
786 <https://doi.org/10.1016/j.agrformet.2021.108509>, 2021.
- 787 Hoose, C., Kristjánsson, J. E., Iversen, T., Kirkevåg, A., Seland, Ø., and Gettelman, A.: Constraining cloud droplet  
788 number concentration in GCMs suppresses the aerosol indirect effect, *Geophys. Res. Lett.*, 36, 2009GL038568,  
789 <https://doi.org/10.1029/2009GL038568>, 2009.
- 790 Horst, T. W.: A Simple Formula for Attenuation of Eddy Fluxes Measured with First-Order Scalar Sensors, *Bound-  
791 Layer Meteorol.*, 82, 219–233, <https://doi.org/10.1023/A:1000229130034>, 1997.
- 792 Intergovernmental Panel on Climate Change (IPCC): Climate Change 2021 – The Physical Science Basis: Working  
793 Group I Contribution to the Sixth Assessment Report of the Intergovernmental Panel on Climate Change, 1st ed.,  
794 Cambridge University Press, <https://doi.org/10.1017/9781009157896>, 2023.
- 795 Islam, M. M., Meskhidze, N., Rasheeda Satheesh, A., and Petters, M. D.: Turbulent Flux Measurements of the Near-  
796 Surface and Residual-Layer Small Particle Events, *J. Geophys. Res. Atmospheres*, 127, e2021JD036289,  
797 <https://doi.org/10.1029/2021JD036289>, 2022.
- 798 Jones, C. R., Bretherton, C. S., and Leon, D.: Coupled vs. decoupled boundary layers in VOCALS-REx, *Atmospheric  
799 Chem. Phys.*, 11, 7143–7153, <https://doi.org/10.5194/acp-11-7143-2011>, 2011.
- 800 Kaimal, J. C. and Finnigan, J. J.: *Atmospheric Boundary Layer Flows: Their Structure and Measurement*, Oxford  
801 University Press, <https://doi.org/10.1093/oso/9780195062397.001.0001>, 1994.
- 802 Koontz, A., Mei, F., and Pekour, M.: aafinletisok.a1, <https://doi.org/10.5439/1241544>, 2016.
- 803 Korolev, A. and Isaac, G. A.: Shattering during Sampling by OAPs and HVPS. Part I: Snow Particles, *J. Atmospheric  
804 Ocean. Technol.*, 22, 528–542, <https://doi.org/10.1175/JTECH1720.1>, 2005.

805 Kuang, C. and Mei, F.: Condensation Particle Counter (CPC) Instrument Handbook - Airborne Version,  
806 <https://doi.org/10.2172/1562676>, 2019.

807 Kulkarni, P. and Wang, J.: New fast integrated mobility spectrometer for real-time measurement of aerosol size  
808 distribution: II. Design, calibration, and performance characterization, *J. Aerosol Sci.*, 37, 1326–1339,  
809 <https://doi.org/10.1016/j.jaerosci.2006.01.010>, 2006a.

810 Kulkarni, P. and Wang, J.: New fast integrated mobility spectrometer for real-time measurement of aerosol size  
811 distribution—I: Concept and theory, *J. Aerosol Sci.*, 37, 1303–1325, <https://doi.org/10.1016/j.jaerosci.2006.01.005>,  
812 2006b.

813 Kulmala, M., Petäjä, T., Nieminen, T., Sipilä, M., Manninen, H. E., Lehtipalo, K., Dal Maso, M., Aalto, P. P.,  
814 Junninen, H., Paasonen, P., Riipinen, I., Lehtinen, K. E. J., Laaksonen, A., and Kerminen, V.-M.: Measurement of the  
815 nucleation of atmospheric aerosol particles, *Nat. Protoc.*, 7, 1651–1667, <https://doi.org/10.1038/nprot.2012.091>, 2012.

816 Lee, X., Massman, W., and Law, B. (Eds.): Handbook of Micrometeorology: A Guide for Surface Flux Measurement  
817 and Analysis, Springer Netherlands, Dordrecht, 250 pp., <https://doi.org/10.1007/1-4020-2265-4>, 2005.

818 Lenschow, D. H. and Stankov, B. B.: Length Scales in the Convective Boundary Layer, *J. Atmospheric Sci.*, 43, 1198–  
819 1209, [https://doi.org/10.1175/1520-0469\(1986\)043<1198:LSITCB>2.0.CO;2](https://doi.org/10.1175/1520-0469(1986)043<1198:LSITCB>2.0.CO;2), 1986.

820 Lenschow, D. H., Wulfmeyer, V., and Senff, C.: Measuring Second- through Fourth-Order Moments in Noisy Data,  
821 *J. Atmospheric Ocean. Technol.*, 17, 1330–1347, [https://doi.org/10.1175/1520-0426\(2000\)017<1330:MSTFOM>2.0.CO;2](https://doi.org/10.1175/1520-0426(2000)017<1330:MSTFOM>2.0.CO;2), 2000.

823 Li, Y., Wu, Y., Tang, J., Zhu, P., Gao, Z., and Yang, Y.: Quantitative Evaluation of Wavelet Analysis Method for  
824 Turbulent Flux Calculation of Non-Stationary Series, *Geophys. Res. Lett.*, 50, e2022GL101591,  
825 <https://doi.org/10.1029/2022GL101591>, 2023.

826 Logan, T., Xi, B., and Dong, X.: Aerosol properties and their influences on marine boundary layer cloud condensation  
827 nuclei at the ARM mobile facility over the Azores, *J. Geophys. Res. Atmospheres*, 119, 4859–4872,  
828 <https://doi.org/10.1002/2013JD021288>, 2014.

829 Lückerrath, J., Held, A., Siebert, H., Michalkow, M., and Wehner, B.: Vertical aerosol particle exchange in the marine  
830 boundary layer estimated from helicopter-borne measurements in the Azores region, *Atmospheric Chem. Phys.*, 22,  
831 10007–10021, <https://doi.org/10.5194/acp-22-10007-2022>, 2022.

832 Martin, S., Beyrich, F., and Bange, J.: Observing Entrainment Processes Using a Small Unmanned Aerial Vehicle: A  
833 Feasibility Study, *Bound.-Layer Meteorol.*, 150, 449–467, <https://doi.org/10.1007/s10546-013-9880-4>, 2014.

834 Mather, J. H. and Voyles, J. W.: The Arm Climate Research Facility: A Review of Structure and Capabilities, *Bull.*  
835 *Am. Meteorol. Soc.*, 94, 377–392, <https://doi.org/10.1175/BAMS-D-11-00218.1>, 2013.

836 Matthews, A. and Goldberger, L.: Aircraft-Integrated Meteorological Measurement System (AIMMS) Instrument  
837 Handbook, <https://doi.org/10.2172/1725866>, 2020.

838 Mei, F. and Gaustad, K.: ARM Aerial Facility (AAF) Merged Value-Added Product Report for Historical G-1 Field  
839 Campaigns, Oak Ridge National Laboratory (ORNL), Oak Ridge, TN (United States). Atmospheric Radiation  
840 Measurement (ARM) Data Center, <https://doi.org/10.2172/2335708>, 2024.

841 Meskhidze, N., Xu, J., Gantt, B., Zhang, Y., Nenes, A., Ghan, S. J., Liu, X., Easter, R., and Zaveri, R.: Global  
842 distribution and climate forcing of marine organic aerosol: 1. Model improvements and evaluation, *Atmospheric*  
843 *Chem. Phys.*, 11, 11689–11705, <https://doi.org/10.5194/acp-11-11689-2011>, 2011.

- 844 Meskhidze, N., Jaimes-Correa, J. C., Petters, M. D., Royalty, T. M., Phillips, B. N., Zimmerman, A., and Reed, R.:  
845 Possible Wintertime Sources of Fine Particles in an Urban Environment, *J. Geophys. Res. Atmospheres*, 124, 13,055-  
846 13,070, <https://doi.org/10.1029/2019JD031367>, 2019.
- 847 Misztal, P. K., Karl, T., Weber, R., Jonsson, H. H., Guenther, A. B., and Goldstein, A. H.: Airborne flux measurements  
848 of biogenic isoprene over California, *Atmospheric Chem. Phys.*, 14, 10631–10647, [https://doi.org/10.5194/acp-14-](https://doi.org/10.5194/acp-14-10631-2014)  
849 10631-2014, 2014.
- 850 Modini, R. L., Ristovski, Z. D., Johnson, G. R., He, C., Surawski, N., Morawska, L., Suni, T., and Kulmala, M.: New  
851 particle formation and growth at a remote, sub-tropical coastal location, *Atmospheric Chem. Phys.*, 9, 7607–7621,  
852 <https://doi.org/10.5194/acp-9-7607-2009>, 2009.
- 853 Nieminen, T., Kerminen, V.-M., Petäjä, T., Aalto, P. P., Arshinov, M., Asmi, E., Baltensperger, U., Beddows, D. C.  
854 S., Beukes, J. P., Collins, D., Ding, A., Harrison, R. M., Henzing, B., Hooda, R., Hu, M., Hörrak, U., Kivekäs, N.,  
855 Komsaare, K., Krejci, R., Kristensson, A., Laakso, L., Laaksonen, A., Leaitch, W. R., Lihavainen, H., Mihalopoulos,  
856 N., Németh, Z., Nie, W., O’Dowd, C., Salma, I., Sellegri, K., Svenningsson, B., Swietlicki, E., Tunved, P., Ulevicius,  
857 V., Vakkari, V., Vana, M., Wiedensohler, A., Wu, Z., Virtanen, A., and Kulmala, M.: Global analysis of continental  
858 boundary layer new particle formation based on long-term measurements, *Atmospheric Chem. Phys.*, 18, 14737–  
859 14756, <https://doi.org/10.5194/acp-18-14737-2018>, 2018.
- 860 Nilsson, E. D., Rannik, Ü., Kulmala, M., Buzorius, G., and O’Dowd, C. D.: Effects of continental boundary layer  
861 evolution, convection, turbulence and entrainment, on aerosol formation, *Tellus Ser. B Chem. Phys. Meteorol. B*, 53,  
862 441–461, <https://doi.org/10.3402/tellusb.v53i4.16617>, 2001.
- 863 O’Dowd, C., Monahan, C., and Dall’Osto, M.: On the occurrence of open ocean particle production and growth events,  
864 *Geophys. Res. Lett.*, 37, 2010GL044679, <https://doi.org/10.1029/2010GL044679>, 2010.
- 865 O’Dowd, C. D., Hämeri, K., Mäkelä, J., Väkeva, M., Aalto, P., de Leeuw, G., Kunz, G. J., Becker, E., Hansson, H.,  
866 Allen, A. G., Harrison, R. M., Berresheim, H., Kleefeld, C., Geever, M., Jennings, S. G., and Kulmala, M.: Coastal  
867 new particle formation: Environmental conditions and aerosol physicochemical characteristics during nucleation  
868 bursts, *J. Geophys. Res. Atmospheres*, 107, <https://doi.org/10.1029/2000JD000206>, 2002.
- 869 Olfert, J. S., Kulkarni, P., and Wang, J.: Measuring aerosol size distributions with the fast integrated mobility  
870 spectrometer, *J. Aerosol Sci.*, 39, 940–956, <https://doi.org/10.1016/j.jaerosci.2008.06.005>, 2008.
- 871 Pekour, M. and Ermold, B.: ARM Aerial Facility (AAF) Merged aerosol size distribution,  
872 <https://doi.org/10.5439/1905541>, 2017.
- 873 Petters, M. D., Snider, J. R., Stevens, B., Vali, G., Faloona, I., and Russell, L. M.: Accumulation mode aerosol, pockets  
874 of open cells, and particle nucleation in the remote subtropical Pacific marine boundary layer, *J. Geophys. Res.*  
875 *Atmospheres*, 111, 2004JD005694, <https://doi.org/10.1029/2004JD005694>, 2006.
- 876 Pirjola, L., O’Dowd, C. D., Brooks, I. M., and Kulmala, M.: Can new particle formation occur in the clean marine  
877 boundary layer?, *J. Geophys. Res. Atmospheres*, 105, 26531–26546, <https://doi.org/10.1029/2000JD900310>, 2000.
- 878 Pope, S. B.: *Turbulent Flows*, 1st ed., Cambridge University Press, <https://doi.org/10.1017/CBO9780511840531>,  
879 2000.
- 880 Pryor, S. C., Larsen, S. E., Sørensen, L. L., Barthelmie, R. J., Grönholm, T., Kulmala, M., Launiainen, S., Rannik, Ü.,  
881 and Vesala, T.: Particle fluxes over forests: Analyses of flux methods and functional dependencies, *J. Geophys. Res.*,  
882 112, D07205, <https://doi.org/10.1029/2006JD008066>, 2007.
- 883 Quinn, P. K., Coffman, D. J., Johnson, J. E., Upchurch, L. M., and Bates, T. S.: Small fraction of marine cloud  
884 condensation nuclei made up of sea spray aerosol, *Nat. Geosci.*, 10, 674–679, <https://doi.org/10.1038/ngeo3003>, 2017.

- 885 Rannik, Ü. and Vesala, T.: Autoregressive filtering versus linear detrending in estimation of fluxes by the eddy  
886 covariance method, *Bound.-Layer Meteorol.*, 91, 259–280, <https://doi.org/10.1023/A:1001840416858>, 1999.
- 887 Sakai, R. K., Fitzjarrald, D. R., and Moore, K. E.: Importance of Low-Frequency Contributions to Eddy Fluxes  
888 Observed over Rough Surfaces, *J. Appl. Meteorol.*, 40, 2178–2192, [https://doi.org/10.1175/1520-0450\(2001\)040<2178:IOLFCT>2.0.CO;2](https://doi.org/10.1175/1520-0450(2001)040<2178:IOLFCT>2.0.CO;2), 2001.
- 890 Schaller, C., Göckede, M., and Foken, T.: Flux calculation of short turbulent events – comparison of three methods,  
891 *Atmospheric Meas. Tech.*, 10, 869–880, <https://doi.org/10.5194/amt-10-869-2017>, 2017.
- 892 Schmid, B., Tomlinson, J. M., Hubbe, J. M., Comstock, J. M., Mei, F., Chand, D., Pekour, M. S., Kluzek, C. D.,  
893 Andrews, E., Biraud, S. C., and McFarquhar, G. M.: The DOE ARM Aerial Facility, *Bull. Am. Meteorol. Soc.*, 95,  
894 723–742, <https://doi.org/10.1175/BAMS-D-13-00040.1>, 2014.
- 895 Siebert, H., Szodry, K.-E., Egerer, U., Wehner, B., Henning, S., Chevalier, K., Lücknerath, J., Welz, O., Weinhold, K.,  
896 Lauermann, F., Gottschalk, M., Ehrlich, A., Wendisch, M., Fialho, P., Roberts, G., Allwayin, N., Schum, S., Shaw,  
897 R. A., Mazzoleni, C., Mazzoleni, L., Nowak, J. L., Malinowski, S. P., Karpinska, K., Kumala, W., Czyzewska, D.,  
898 Luke, E. P., Kollias, P., Wood, R., and Mellado, J. P.: Observations of Aerosol, Cloud, Turbulence, and Radiation  
899 Properties at the Top of the Marine Boundary Layer over the Eastern North Atlantic Ocean: The ACORES Campaign,  
900 *Bull. Am. Meteorol. Soc.*, 102, E123–E147, <https://doi.org/10.1175/BAMS-D-19-0191.1>, 2021.
- 901 Spirig, C., Neftel, A., Ammann, C., Dommen, J., Grabmer, W., Thielmann, A., Schaub, A., Beauchamp, J., Wisthaler,  
902 A., and Hansel, A.: Eddy covariance flux measurements of biogenic VOCs during ECHO 2003 using proton transfer  
903 reaction mass spectrometry, *Atmospheric Chem. Phys.*, 5, 465–481, <https://doi.org/10.5194/acp-5-465-2005>, 2005.
- 904 Stull, R. B. (Ed.): *An Introduction to Boundary Layer Meteorology*, Springer Netherlands, Dordrecht,  
905 <https://doi.org/10.1007/978-94-009-3027-8>, 1988.
- 906 Sun, Y., Jia, L., Chen, Q., and Zheng, C.: Optimizing Window Length for Turbulent Heat Flux Calculations from  
907 Airborne Eddy Covariance Measurements under Near Neutral to Unstable Atmospheric Stability Conditions, *Remote  
908 Sens.*, 10, 670, <https://doi.org/10.3390/rs10050670>, 2018.
- 909 Torrence, C. and Compo, G. P.: A Practical Guide to Wavelet Analysis., *Bull. Am. Meteorol. Soc.*, 79, 61–78,  
910 [https://doi.org/10.1175/1520-0477\(1998\)079<0061:APGTWA>2.0.CO;2](https://doi.org/10.1175/1520-0477(1998)079<0061:APGTWA>2.0.CO;2), 1998.
- 911 Wang, J., Pikridas, M., Spielman, S. R., and Pinterich, T.: A fast integrated mobility spectrometer for rapid  
912 measurement of sub-micrometer aerosol size distribution, Part I: Design and model evaluation, *J. Aerosol Sci.*, 108,  
913 44–55, <https://doi.org/10.1016/j.jaerosci.2017.02.012>, 2017a.
- 914 Wang, J., Pikridas, M., Pinterich, T., Spielman, S. R., Tsang, T., McMahon, A., and Smith, S.: A Fast Integrated  
915 Mobility Spectrometer for rapid measurement of sub-micrometer aerosol size distribution, Part II: Experimental  
916 characterization, *J. Aerosol Sci.*, 113, 119–129, <https://doi.org/10.1016/j.jaerosci.2017.05.001>, 2017b.
- 917 Wang, J., Wood, R., Jensen, M., Azevedo, E., Bretherton, C., and Chand, D.: Aerosol and Cloud Experiments in  
918 Eastern North Atlantic (ACE-ENA) Field Campaign Report, 2019.
- 919 Weber, R. J., Marti, J. J., McMurry, P. H., Eisele, F. L., Tanner, D. J., and Jefferson, A.: Measurements of new particle  
920 formation and ultrafine particle growth rates at a clean continental site, *J. Geophys. Res. Atmospheres*, 102, 4375–  
921 4385, <https://doi.org/10.1029/96JD03656>, 1997.
- 922 Weber, R. J., Clarke, A. D., Litchy, M., Li, J., Kok, G., Schillawski, R. D., and McMurry, P. H.: Spurious aerosol  
923 measurements when sampling from aircraft in the vicinity of clouds, *J. Geophys. Res. Atmospheres*, 103, 28337–  
924 28346, <https://doi.org/10.1029/98JD02086>, 1998.

925 Wiedensohler, A., Covert, D. S., Swietlicki, Erik., Aalto, Pasi., Heintzenberg, Jost., and Leck, C.: Occurrence of an  
926 ultrafine particle mode less than 20 nm in diameter in the marine boundary layer during Arctic summer and autumn,  
927 *Tellus B*, 48, 213–222, <https://doi.org/10.1034/j.1600-0889.1996.t01-1-00006.x>, 1996.

928 Wolfe, G. M., Kawa, S. R., Hanisco, T. F., Hannun, R. A., Newman, P. A., Swanson, A., Bailey, S., Barrick, J.,  
929 Thornhill, K. L., Diskin, G., DiGangi, J., Nowak, J. B., Sorenson, C., Bland, G., Yungel, J. K., and Swenson, C. A.:  
930 The NASA Carbon Airborne Flux Experiment (CARAFE): instrumentation and methodology, *Atmospheric Meas.*  
931 *Tech.*, 11, 1757–1776, <https://doi.org/10.5194/amt-11-1757-2018>, 2018.

932 Wood, R. and Bretherton, C. S.: Boundary Layer Depth, Entrainment, and Decoupling in the Cloud-Capped  
933 Subtropical and Tropical Marine Boundary Layer, *J. Clim.*, 17, 3576–3588, [https://doi.org/10.1175/1520-0442\(2004\)017<3576:BLDEAD>2.0.CO;2](https://doi.org/10.1175/1520-0442(2004)017<3576:BLDEAD>2.0.CO;2), 2004.

935 Wood, R., Wyant, M., Bretherton, C. S., Rémillard, J., Kollias, P., Fletcher, J., Stemmler, J., de Szoeki, S., Yuter, S.,  
936 Miller, M., Mechem, D., Tselioudis, G., Chiu, J. C., Mann, J. A. L., O’Connor, E. J., Hogan, R. J., Dong, X., Miller,  
937 M., Ghate, V., Jefferson, A., Min, Q., Minnis, P., Palikonda, R., Albrecht, B., Luke, E., Hannay, C., and Lin, Y.:  
938 Clouds, Aerosols, and Precipitation in the Marine Boundary Layer: An Arm Mobile Facility Deployment, *Bull. Am.*  
939 *Meteorol. Soc.*, 96, 419–440, <https://doi.org/10.1175/BAMS-D-13-00180.1>, 2015.

940 Wulfmeyer, V., Muppa, S. K., Behrendt, A., Hammann, E., Späth, F., Sorbjan, Z., Turner, D. D., and Hardesty, R.  
941 M.: Determination of Convective Boundary Layer Entrainment Fluxes, Dissipation Rates, and the Molecular  
942 Destruction of Variances: Theoretical Description and a Strategy for Its Confirmation with a Novel Lidar System  
943 Synergy, *J. Atmospheric Sci.*, 73, 667–692, <https://doi.org/10.1175/JAS-D-14-0392.1>, 2016.

944 Zhang, J., Chen, Y.-S., Yamaguchi, T., and Feingold, G.: Cloud water adjustments to aerosol perturbations are  
945 buffered by solar heating in non-precipitating marine stratocumuli, *Atmospheric Chem. Phys.*, 24, 10425–10440,  
946 <https://doi.org/10.5194/acp-24-10425-2024>, 2024.

947 Zheng, G., Wang, Y., Aiken, A. C., Gallo, F., Jensen, M. P., Kollias, P., Kuang, C., Luke, E., Springston, S., Uin, J.,  
948 Wood, R., and Wang, J.: Marine boundary layer aerosol in the eastern North Atlantic: seasonal variations and key  
949 controlling processes, *Atmospheric Chem. Phys.*, 18, 17615–17635, <https://doi.org/10.5194/acp-18-17615-2018>,  
950 2018.

951 Zheng, G., Wang, Y., Wood, R., Jensen, M. P., Kuang, C., McCoy, I. L., Matthews, A., Mei, F., Tomlinson, J. M.,  
952 Shilling, J. E., Zawadowicz, M. A., Crosbie, E., Moore, R., Ziemba, L., Andreae, M. O., and Wang, J.: New particle  
953 formation in the remote marine boundary layer, *Nat. Commun.*, 12, 527, <https://doi.org/10.1038/s41467-020-20773-1>,  
954 2021.

955